

1 **Probabilistic Hierarchical Interpolation and Interpretable Configuration for Flood Prediction**

2 Mostafa Saberian¹, Vidya Samadi^{2*}, Ioana Popescu³

3 1. The Glenn Department of Civil Engineering, Clemson University, Clemson, SC

4 2. Department of Agricultural Sciences, Clemson University, Clemson, SC.

5 3. Department of Hydroinformatics and Socio-Technical Innovation, IHE Delft Institute for Water
6 Education, Delft, the Netherlands

7 *Corresponding author: samadi@clemson.edu

8 **Abstract**

9 The last few years have witnessed the rise of neural networks (NNs) applications for hydrological time
10 series modeling. By virtue of their capabilities, NN models can achieve unprecedented levels of
11 performance when learn how to solve increasingly complex rainfall-runoff processes via data, making them
12 pivotal for the development of computational hydrologic tasks such as flood predictions. The NN models
13 should, in order to be considered practical, provide a probabilistic understanding of the model mechanisms
14 and predictions and hints on what could perturb the model. In this paper, we developed two **probabilistic**
15 NN models, i.e., Neural Hierarchical Interpolation for Time Series Forecasting (N-HiTS) and Network-
16 Based Expansion Analysis for Interpretable Time Series Forecasting (N-BEATS) **with a probabilistic**
17 **multi-quantile objective** and benchmarked them with long short-term memory (LSTM) for flood
18 prediction across two headwater streams in Georgia and North Carolina, USA. To generate a probabilistic
19 prediction, a Multi-Quantile Loss was used to assess the 95th percentile prediction uncertainty (95PPU) of
20 multiple flooding events. **Extensive experiments demonstrated We conducted extensive flood prediction**
21 **experiments demonstrating** the advantages of hierarchical interpolation and interpretable architecture,
22 where both N-HiTS and N-BEATS provided an average accuracy improvement of **$\sim 5\%$ almost 5% (NSE)**
23 over the LSTM benchmarking model. On a variety of flooding events, both N-HiTS and N-BEATS
24 demonstrated significant performance improvements over the LSTM benchmark and showcased their
25 probabilistic predictions by specifying a likelihood **parameter objective**.

Formatted: Font: (Default) +Headings CS (Times New Roman), 11 pt, Font color: Auto

26

27 **Keywords:** Probabilistic Flood Prediction; Neural Networks; N-HiTS; N-BEATS; LSTM; Headwater
28 Stream.

29 **Key Points**

- 30 • N-HiTS and N-BEATS predictions reflect interpretability and hierarchical representations of data
31 to reduce neural network complexities.

- 32 • Both N-HiTS and N-BEATS models outperformed the LSTM in mathematically defining
33 uncertainty bands.
34 • Predicting the magnitude of the recession curve of flood hydrographs was particularly challenging
35 for all models.

36 **Plain Language Summary**

37 Recent progress in NN accelerated improvements in the performance of catchment modeling. Yet flood
38 modeling remains a very difficult task. Focusing on two headwater streams, we developed N-HiTS and N-
39 BEATS models and benchmarked them with LSTM to predict flooding. N-HiTS and N-BEATS
40 outperformed LSTM for flood predictions. We demonstrated how the proposed models can be augmented
41 with an uncertainty approach to predict flooding that is interpretable without considerable loss in accuracy.
42

43 **1. Introduction**

44 The ~~last past~~ few years ~~have witnessed a rapid surge have been character an upsurge~~ in the neural networks
45 (NN) applications in hydrology. ~~As these opaque, data-driven models are increasingly employed for critical~~
46 ~~hydrological predictions, the hydrology community has placed growing emphasis on developing~~
47 ~~trustworthy and interpretable NN models. As opaque NN models are increasingly being emp.~~ However,
48 maintaining coherence while producing accurate predictions can be a challenging problem (Olivares et al.,
49 2024). There is a general agreement on the importance of providing probabilistic NN prediction (Sadeghi
50 and Samadi, 2024), especially in the case of flood prediction (Martinaitis et al., 2023).

51 Flood occurrences have witnessed an alarming surge in frequency and severity globally. Jonkman (2005)
52 studied a natural disaster database (EM-DAT, 2023) and reported that over 27 years, more than 175000
53 people died, and close to 2.2 billion were affected directly by floods worldwide. These numbers are likely
54 an underestimation due to unreported events (Nevo et al., 2022). In addition, the United Nations Office for
55 Disaster Risk Reduction reported that flooding has been the most frequent, widespread weather-related
56 natural disaster since 1995, claiming over 600,000 lives, affecting around 4 billion people globally, and
57 causing annual economic damage of more than 100 billion USD (UNISDR, 2015). This escalating trend
58 has necessitated the need for better flood prediction and management strategies. Scholars have successfully
59 implemented different flood models such as deterministic (e.g., Roelvink et al., 2009, Thompson and
60 Frazier, 2014; Barnard et al., 2014; Erikson et al., 2018) and physically based flood models (e.g., Basso et
61 al., 2016; Chen et al., 2016; Pourreza-Bilondi et al., 2017; Saksena et al., 2019; Refsgaard et al., 2021) in
62 various environmental systems over the past several decades. These studies have heightened the need for
63 precise flood prediction (Samadi et al., 2025), they have also unveiled limitations inherent in existing
64 deterministic and physics-based models. While evidence suggests that both deterministic and physics-based

Formatted: Font: Not Bold

65 approaches are meaningful and useful (Sukovich et al., 2014; Zafarmomen et al., 2024), their forecasts rest
66 heavily on imprecise and subjective expert opinion; there is a challenge for setting robust evidence-based
67 thresholds to issue flood warnings and alerts (Palmer, 2012). Moreover, many of these traditional flood
68 models particularly physically explicit ~~models~~models, rely heavily on a particular choice of numerical
69 approximation and describe multiple process parameterizations only within a fixed spatial architecture (e.g.,
70 Clark et al., 2015). Recent NN models have shown promising results across a large variety of flood
71 modeling applications (e.g., Nevo et al., 2022; Pally and Samadi, 2022; Dasgupta et al., 2023; Zhang et al.,
72 2023; Zafarmomen and Samadi, 2025; Saberian et al., 2025) and encourage the use of such methodologies
73 as core drivers for neural flood prediction (Windheuser et al., 2023).
74 Earlier adaptations of these intelligent techniques showed promising for flood prediction (e.g., Hsu et al.,
75 1995; Tiwari and Chatterjee, 2010). However, recent efforts have taken NN application to the next level,
76 providing uncertainty assessment (Sadeghi Tabas and Samadi, 2022) and improvements over various
77 spatio-temporal scales, regions, and processes (e.g., Kratzert et al., 2018; Park and Lee, 2023; Zhang et al.,
78 2023). Nevo et al., (2022) were the first scholars who employed long short-term memory (LSTM) for flood
79 stage prediction and inundation mapping, achieving notable success during the 2021 monsoon season. Soon
80 after, Russo et al. (2023) evaluated various NN models for predicting flood depth in urban systems,
81 highlighting the potential of data-driven models for urban flood prediction. Similarly, Defontaine et al.
82 (2023) emphasized the role of NN algorithms in enhancing the reliability of flood predictions, particularly
83 in the context of limited data availability. Windheuser et al., (2023) studied flood gauge height forecasting
84 using images and time series data for two gauging stations in Georgia, USA. They used multiple NN models
85 such as Convolutional Neural Network (ConvNet/CNN) and LSTM to forecast floods in near real-time (up
86 to 72 hours). In a sequence, Wee et al., (2023) used Impact-Based Forecasting (IBF) to propose a Flood
87 Impact-Based Forecasting system (FIBF) using flexible fuzzy inference techniques, aiding decision-makers
88 in a timely response. Zou et al. (2023) proposed a Residual LSTM (ResLSTM) model to enhance and
89 address flood prediction gradient issues. They integrated Deep Autoregressive Recurrent (DeepAR) with
90 four recurrent neural networks (RNNs), including ResLSTM, LSTM, Gated Recurrent Unit (GRU), and
91 Time Feedforward Connections Single Gate Recurrent Unit (TFC-SGRU). They showed that ResLSTM
92 achieved superior accuracy. While these studies reported the superiority of NN models for flood modeling,
93 they highlighted a number of challenges, notably (i) the limited capability of proposed NN models to
94 capture the spatial variability and magnitudes of extreme data over time, (ii) the lack of a sophisticated
95 mechanism to capture different flood magnitudes and synthesize the prediction, and (iii) inability of the NN
96 models to process data in parallel and capture the relationships between all elements in a sequential manner.
97 Recent advances in neural time series forecasting showed promising results that can be used to address the
98 above challenges for flood prediction. Recent techniques include the adoption of the attention mechanism

99 and Transformer-inspired approaches (Fan et al. 2019; Alaa and van der Schaar 2019; Lim et al. 2021)
100 along with attention-free architectures composed of deep stacks of fully connected layers (Oreshkin et al.
101 2020). All of these approaches are relatively easy to scale up in terms of flood magnitudes (small to major
102 flood predictions), compared to LSTM and have proven to be capable of capturing spatiotemporal
103 dependencies (Challu et al., 2022). In addition, these architectures can capture input-output relationships
104 implicitly while they tend to be more computationally efficient. Many state-of-the-art NN approaches for
105 flood forecasting have been established based on LSTM. There are cell states in the LSTM networks that
106 can be interpreted as storage capacity often used in flood generation schemes. In LSTM, the updating of
107 internal cell states (or storages) is regulated through a number of gates: the first gate regulates the storage
108 depletion, the second one regulates storage fluctuations, and the third gate regulates the storages outflow
109 (Tabas and Samadi, 2022). The elaborate gated design of the LSTM partly solves the long-term dependency
110 problem in flood time series prediction (Fang et al., 2020), although, the structure of LSTMs is designed in
111 a sequential manner that cannot directly connect two nonadjacent portions (positions) of a time series.

112 In this paper, we developed attention-free architecture, i.e. Neural Hierarchical Interpolation for Time
113 Series Forecasting (N-HiTS; Challu et al., 2022) and Network-Based Expansion Analysis for Interpretable
114 Time Series Forecasting (N-BEATS; Oreshkin et al., 2020) and benchmarked these models with LSTM for
115 flood prediction. We developed fully connected N-BEATS and N-HiTS architectures using multi-rate data
116 sampling, synthesizing the flood prediction outputs via multi-scale interpolation.

117 We implemented all algorithms for flood prediction on two headwater streams i.e., the Lower Dog River,
118 Georgia, and the Upper Dutchmans Creek, North Carolina, USA to ensure that the results are reliable and
119 comparable. The results of N-BEATS and N-HiTS techniques were compared with the benchmarking
120 LSTM to understand how these techniques can improve the representations of rainfall and runoff
121 dispensing over a recurrence process. Notably, this study represents a pioneering effort, as to the best of
122 our knowledge, this is the first instance in which the application of N-BEATS and N-HiTS algorithms in
123 the field of flood prediction has been explored. The scope of this research will focus on:

124
125 (i) **Flood prediction in a hierarchical fashion with interpretable outputs:** We built N-BEATS and
126 N-HiTS for flood prediction with a very deep stack of fully connected layers to implicitly capture input-
127 output relationships with hierarchical interpolation capabilities. The predictions also involve programming
128 the algorithms with decreasing complexity and aligning their time scale with the final output through multi-
129 scale hierarchical interpolation and interpretable architecture. Predictions were aggregated in a hierarchical
130 fashion that enabled the building of a very deep neural network with interpretable configurations.

131 (ii) **Uncertainty quantification of the models by employing probabilistic approaches:** a Multi-
132 Quantile Loss (MQL) was used to assess the 95th percentile prediction uncertainty (95PPU) of multiple

133 flooding events. MQL was integrated as the loss function to account for probabilistic prediction. MQL
134 trains the model to produce probabilistic forecasts by predicting multiple quantiles of the distribution of
135 future values.

136 **(iii) Exploring headwater stream response to flooding:** Understanding the dynamic response of
137 headwater streams to flooding is essential for managing downstream flood risks. Headwater streams
138 constitute the uppermost sections of stream networks, usually comprising 60% to 80% of a catchment area.
139 Given this substantial coverage and the tendency for precipitation to increase with elevation, headwater
140 streams are responsible for generating and controlling the majority of runoff in downstream portions
141 (MacDonald and Coe, 2007).

142 The remainder of this paper is structured as follows. Section 2 presents the case study and data, NN models,
143 performance metrics, and sensitivity and uncertainty approaches. Section 3 focuses on the results of flood
144 predictions including sensitivity and uncertainty assessment and computation efficiency. Finally, Section 4
145 concludes the paper.

146

147 **2. Methodology**

148 **2.1. Case Study and Data**

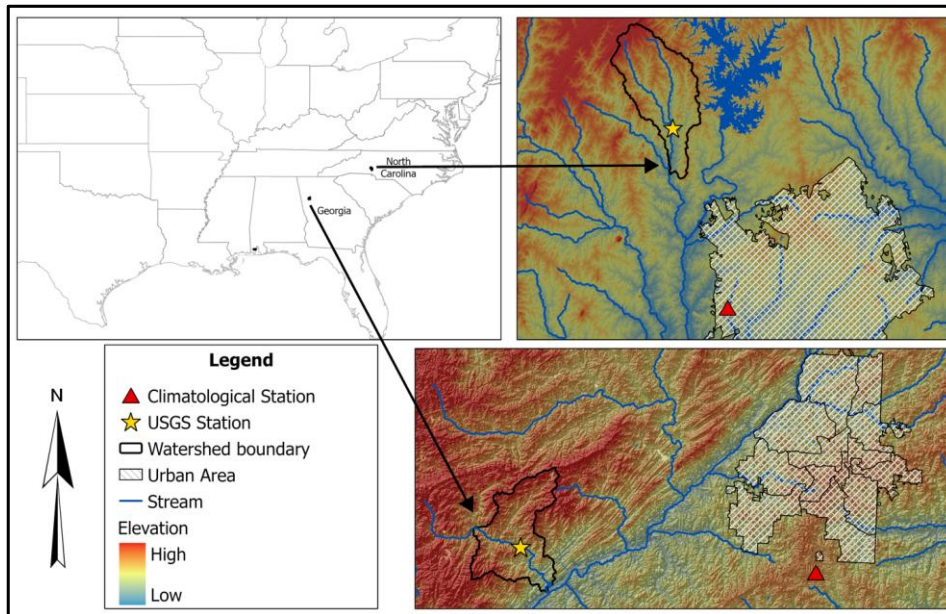
149 This research used two headwater gauging stations located at the Lower Dog River watershed, Georgia
150 (GA; USGS02337410, Dog River gauging station), and the Upper Dutchmans Creek watershed, North
151 Carolina (NC; USGS0214269560, Killian Creek gauging station). As depicted in Figures 1 and 2, the Lower
152 Dog River and the Upper Dutchmans Creek watersheds are located in the west and north parts of two
153 metropolitan cities, Atlanta and Charlotte. As shown in Figure 1, The Lower Dog River stream gauge is
154 established southeast of Villa Rica in Carroll County, where the USGS has regularly monitored discharge
155 data since 2007 in 15-minute increments. The Lower Dog River is a stream with a length of 15.7 miles
156 (25.3 km; obtained from the U.S. Geological Survey [USGS] National Hydrography Dataset high-
157 resolution flowline data), an average elevation of 851.94 meters, and the watershed area above this gauging
158 station is 66.5 square miles (172 km²; obtained from the Georgia Department of Natural Resources). This
159 watershed is covered by 15.2% residential area, 14.6% agricultural land, and ~70% forest (Munn et al.,
160 2020). Killian Creek gauging station at the Upper Dutchmans Creek watershed is established
161 in Montgomery County, NC, where the USGS has regularly monitored discharge data since 1995 in 15-
162 minute increments. The Upper Dutchmans Creek is a stream with a length of 4.9 miles (7.9 km), an average
163 elevation of 642.2 meters (see Table 1), and the watershed area above this gauging station is 4 square miles
164 (10.3 km²) with less than 3% residential area and about 93% forested land use (the United States
165 Environmental Protection Agency).

166 The Lower Dog River has experienced significant flooding in the last decades. For example, in September
167 2009, the creek, along with most of northern GA, experienced heavy rainfall (5 inches, equal to 94 mm).
168 The Lower Dog River, overwhelmed by large amounts of overland flow from saturated ground in the
169 watershed, experienced massive flooding in September 2009 (Gotvald, 2010). The river crested at 33.8 feet
170 (10.3 m) with a peak discharge of 59,900 cfs (1,700 m³/s), nearly six times the 100-year flood level
171 (McCallum and Gotvald, 2010). In addition, Dutchmans Creek has experienced significant flooding in
172 February 2020. According to local news (WCCB Charlotte, 2020), the flood in Gaston County caused
173 significant infrastructure damage and community disruption. Key impacts included the threatened collapse
174 of the Dutchman's Creek bridge in Mt. Holly and the closure of Highway 7 in McAdenville, GA.
175

176 Table 1. The Lower Dog River and Upper Dutchmans Creek's physical characteristics.

Watershed	USGS Station ID Number	Average Elevation (m)	Stream Length (km)	Watershed area (km ²)
Lower Dog River watershed, GA	USGS02337410	851.9	25.3	172
Upper Dutchmans Creek watershed, NC	USGS0214269560	642.2	7.9	10.3

177



179 Figure 1. The Lower Dog River and The Upper Dutchmans Creek watersheds are located in GA and NC.
180 The proximity of the watersheds to Atlanta and Charlotte (urban area) are also displayed on the map.

181
182 To provide the meteorological forcing data, i.e., precipitation, temperature, and humidity, were extracted
183 from the National Oceanic and Atmospheric Administration's (NOAA) Local Climatological Data
184 (LCD). We used the NOAA precipitation, temperature, and humidity data of Atlanta Hartsfield Jackson
185 International Airport and Charlotte Douglas Airport stations as an input variable for neural network
186 algorithms. The data has been monitored since January 1, 1948, and July 22, 1941, with an hourly interval
187 which was used as an input variable for constructing neural networks.

188 To fill in the missing values in the data, we used the spline interpolation method. We applied this method
189 to fill the gaps in time series data, although the missing values were insignificant (less than 1%). In addition,
190 we employed the Minimum Inter-Event Time (MIT) approach to precisely identify and separate individual
191 storm events. The MIT-based event delineation is pivotal for accurately defining storm events. This method
192 allowed us to isolate discrete rainfall episodes, aiding a comprehensive analysis of storm events. Moreover,
193 it provided a basis for event-specific examination of flood responses, such as initial condition and cessation
194 (loss), runoff generation, and runoff dynamics.

195 The hourly rainfall dataset consists of distinct rainfall occurrences, some consecutive and others clustered
196 with brief intervals of zero rainfall. As these zero intervals extend, we aim to categorize them into distinct
197 events. It's worth noting that even within a single storm event, we often encounter short periods of no
198 rainfall, known as intra-storm zero values. In the MIT method, we defined a storm event as a discrete rainfall
199 episode surrounded by dry periods both preceding and following it, determined by an MIT (Asquith et al.,
200 2005; Safaei-Moghadam et al., 2023). There are many means to determine an MIT value. One practical
201 approximation is using serial autocorrelation between rainfall occurrences. MIT approach uses
202 autocorrelation that measures the statistical dependency of rainfall data at one point in time with data at
203 earlier, or lagged times within the time series. The lag time represents the gap between data points being
204 correlated. When the lag time is zero, the autocorrelation coefficient is unity, indicating a one-to-one
205 correlation. As the lag time increases, the statistical correlation diminishes, converging to a minimum value.
206 This signifies the fact that rainfall events become progressively less statistically dependent or, in other
207 words, temporally unrelated. To pinpoint the optimal MIT, we analyzed the autocorrelation coefficients for
208 various lag times, observing the point at which the coefficient approaches zero. This lag time signifies the
209 minimum interval of no rainfall, effectively delineating distinct rainfall events.

210 **2.2. NN Algorithms**

211 In this study, three distinct neural network (NN) architectures were developed to perform multi-horizon
212 flood forecasting. Each NN was coupled with a MQL objective to generate probabilistic predictions and
213 quantify predictive uncertainty. Throughout the manuscript, the term parameters are used exclusively to
214 refer to the network's weights and biases for clarity and consistency.

215 **2.2.1. LSTM**

216 LSTM is an RNN architecture widely used as a benchmark model for flood neural time series
217 modeling. LSTM networks are capable of selectively learning order dependence in sequence prediction
218 problems (Sadeghi Tabas and Samadi, 2022). These networks are powerful because they can capture the
219 temporal features, especially the long-term dependencies (Hochreiter et al., 2001), and are independent of
220 the length of the input data sequences meaning that each sample is independent from another one.

221 The memory cell state within LSTM plays a crucial role in capturing extended patterns in data, making it
222 well-suited for dynamic time series modeling such as flood prediction. An LSTM cell uses the following
223 functions to compute flood prediction.

$$i_t = \sigma(A_i x_t + B_i h_{t-1} + c_i) \quad (\text{Equation 1})$$

$$f_t = \sigma(A_f x_t + B_f h_{t-1} + c_f) \quad (\text{Equation 2})$$

$$o_t = \sigma(A_o x_t + B_o h_{t-1} + c_o) \quad (\text{Equation 3})$$

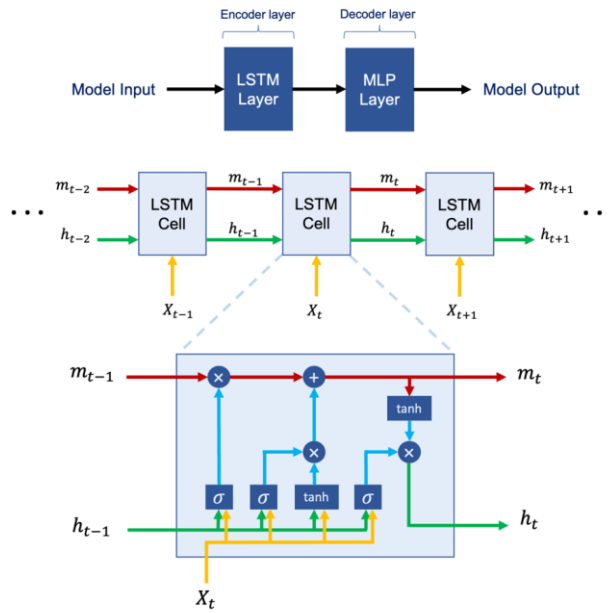
$$m_t = f_t \odot m_{t-1} + i_t \odot \tanh(A_g x_t + B_g h_{t-1} + c_g) \quad (\text{Equation 4})$$

$$h_t = o_t \odot \tanh(m_t) \quad (\text{Equation 5})$$

224 Where x_t and h_t represent the input and the hidden state at time step t , respectively. \odot denotes element-
225 wise multiplication, \tanh stands for the hyperbolic tangent activation function, and σ represents the
226 sigmoid activation function. A , B , and c are trainable weights and biases that undergo optimization during
227 the training process. m_t and h_t are cell states at time step t that are employed in the input processing for
228 the next time step. m_t represents the memory state responsible for preserving long-term information, while
229 h_t represents the memory state preserving short-term information. The LSTM cell consists of a forget gate
230 f_t , an input gate i_t and an output gate o_t and has a cell state m_t . At every time step t , the cell gets the data
231 point x_t with the output of the previous cell h_{t-1} (Windheuser et al., 2023). The forget gate then defines if
232 the information is removed from the cell state, while the input gate evaluates if the information should be

233 added to the cell state and the output gate specifies which information from the cell state can be used for
 234 the next cells.

235 We used two LSTM layers with 128 cells in the first two hidden layers as encoder layers, which were then
 236 connected to two multilayer perceptron (MLP) layers with 128 neurons as decoder layers. The LSTM
 237 simulation was performed with these input layers along with the *Adam* optimizer (Kingma and Ba,
 238 2014), *tanh* activation function, and a single lagged dependent-variable value to train with a learning rate
 239 of 0.001. The architecture of the proposed LSTM model is illustrated in Figure 2.



240
 241 Figure 2. The structure of LSTM programmed in this research. We used *tanh* and *sigmoid* as activation
 242 functions along with 2 layers of LSTM, 2 layers of MLP, and 128 cells in each layer.
 243

244 2.2.2. N-BEATS

245 N-BEATS is a deep learning architecture based on backward and forward residual links and the very deep
 246 stack of fully connected layers specifically designed for sequential data forecasting tasks (Oreshkin et al.,
 247 2020). This architecture has a number of desirable properties including interpretability. The N-BEATS
 248 architecture distinguishes itself from existing architectures in several ways. First, the algorithm approaches

249 forecasting as a non-linear multivariate regression problem instead of a sequence-to-sequence
250 challenge. Indeed, the core component of this architecture (as depicted in Figure 3) is a fully connected
251 non-linear regressor, which takes the historical data from a time series as input and generates multiple data
252 points for the forecasting horizon. Second, the majority of existing time series architectures are quite limited
253 in depth, typically consisting of one to five LSTM layers. N-BEATS employs the residual principle to stack
254 a substantial number of layers together, as illustrated in Figure 3. In this configuration, the basic block not
255 only predicts the next output but also assesses its contribution to decomposing the input, a concept that is
256 referred to as "backcast" (see Oreshkin et al. 2020).

257 The basic building block in the architecture features a fork-like structure, as illustrated in Figure 3 (bottom).
258 The l -th block (for the sake of brevity, the block index l is omitted from Figure 3) takes its respective input,
259 x_l , and produces two output vectors: \hat{x}_l and \hat{y}_l . In the initial block of the model, x_l corresponds to the
260 overall model input, which is a historical lookback window of a specific length, culminating with the most
261 recent observed data point. For the subsequent blocks, x_l is derived from the residual outputs of the
262 preceding blocks. Each block generates two distinct outputs: 1. \hat{y}_l : This represents the forward forecast of
263 the block, spanning a duration of H time units. 2. \hat{x}_l : This signifies the block's optimal estimation of x_l ,
264 which is referred to "backcast." This estimation is made within the constraints of the functional space
265 available to the block for approximating signals (Oreshkin et al., 2020).

266 Internally, the fundamental building block is composed of two elements. The initial element involves a
267 fully connected network, which generates forward expansion coefficient predictors, θ_l^f , and a backward
268 expansion coefficient predictor, θ_l^b . The second element encompasses both backward basis layers, g_l^b , and
269 forward basis layers, g_l^f . These layers take the corresponding forward θ_l^f and backward θ_l^b expansion
270 coefficients as input, conduct internal transformations using a set of basis functions, and ultimately yield
271 the backcast, \hat{x}_l , and the forecast outputs, \hat{y}_l , as previously described by Oreshkin et al. (2020). The
272 following equations describe the first element:

$$h_{l,1} = FC_{l,1}(x_l), \quad h_{l,2} = FC_{l,2}(h_{l,1}), \quad h_{l,3} = FC_{l,3}(h_{l,2}), \quad h_{l,4} = FC_{l,4}(h_{l,3}). \quad (\text{Equation 6})$$

$$\theta_l^b = \text{LINEAR}_l^b(h_{l,4}), \quad \theta_l^f = \text{LINEAR}_l^f(h_{l,4}) \quad (\text{Equation 7})$$

273 The LINEAR layer, in essence, functions as a straightforward linear projection, meaning $\theta_l^f = W_l^f h_{l,4}$. As
274 for the fully connected (FC) layer, it takes on the role of a conventional FC layer, incorporating RELU non-
275 linearity as an activation function.

276 The second element performs the mapping of expansion coefficients θ_l^f and θ_l^b to produce outputs using
 277 basis layers, resulting in $\hat{y}_l = g_l^f(\theta_l^f)$ and $\hat{x}_l = g_l^b(\theta_l^b)$. This process is defined by the following equation:

$$\hat{y}_l = \sum_{i=1}^{\dim(\theta_l^f)} \theta_{l,i}^f v_i^f, \quad \hat{x}_l = \sum_{i=1}^{\dim(\theta_l^b)} \theta_{l,i}^b v_i^b \quad (\text{Equation 8})$$

278 Within this context, v_i^f and v_i^b represent the basis vectors for forecasting and backcasting, respectively,
 279 while $\theta_{l,i}^f$ corresponds to the i -th element of θ_l^f .

280 The N-BEATS uses a novel hierarchical doubly residual architecture which is illustrated in Figure 3 (top
 281 and middle). This framework incorporates two residual branches, one traversing the backcast predictions
 282 of each layer, while the other traverses the forecast branch of each layer. The following equation describes
 283 this process:

$$x_l = x_{l-1} - \hat{x}_{l-1} \quad , \quad \hat{y} = \sum_l \hat{y}_l \quad (\text{Equation 9})$$

284 As mentioned earlier, in the specific scenario of the initial block, its input corresponds to the model-level
 285 input x . In contrast, for all subsequent blocks, the backcast residual branch x_l can be conceptualized as
 286 conducting a sequential analysis of the input signal. The preceding block eliminates the portion of the signal
 287 \hat{x}_{l-1} that it can effectively approximate, thereby simplifying the prediction task for downstream blocks.
 288 Significantly, each block produces a partial forecast \hat{y}_l , which is initially aggregated at the stack level and
 289 subsequently at the overall network level, establishing a hierarchical decomposition. The ultimate forecast
 290 \hat{y} is the summation of all partial forecasts (Oreshkin et al., 2020).

291 The N-BEATS model has two primary configurations: generic and interpretable. These configurations
 292 determine how the model structures its blocks and how it processes time series data. In the generic
 293 configuration, the model uses a stack of generic blocks that are designed to be flexible and adaptable to
 294 various patterns in the time series data. Each generic block consists of fully connected layers with ReLU
 295 activation functions. The key characteristic of the generic configuration is its flexibility. Since the blocks
 296 are not specialized for any specific pattern (like trend or seasonality), they can learn a wide range of patterns
 297 directly from the data (Oreshkin et al., 2020). In the interpretable configuration, the model architecture
 298 integrates distinct trend and seasonality components. This involves structuring the basis layers at the stack
 299 level specifically to model these elements, allowing the stack outputs to be more easily understood.

300 **Trend Model:** In this stack $g_{s,l}^b$ and $g_{s,l}^f$ are polynomials of a small degree p , functions that vary slowly
301 across the forecast window, to replicate monotonic or slowly varying nature of trends:

$$\hat{y}_{s,l} = \sum_{i=0}^p \theta_{s,l,i}^f t^i \quad (\text{Equation 10})$$

302 The time vector $t = [0, 1, 2, \dots, H-2, H-1]^T/H$ is specified on a discrete grid ranging from 0 to
303 $(H-1)/H$, projecting H steps into the future. Consequently, the trend forecast represented in matrix form is:

$$\hat{y}_{s,l}^{tr} = T \theta_{s,l}^f \quad (\text{Equation 11})$$

304 Where the polynomial coefficients, $\theta_{s,l}^f$, predicted by an FC network at layer l of stack s , are described by
305 Equations (6) and (7). The matrix T , consisting of powers of t , is represented as $[1, t, \dots, t^p]$. When p is
306 small, such as 2 or 3, it compels $\hat{y}_{s,l}^{tr}$ to emulate a trend (Oreshkin et al., 2020).

307 Seasonality model: In this stack $g_{s,l}^b$ and $g_{s,l}^f$ are periodic functions, to capture the cyclical and recurring
308 characteristics of seasonality, such that $y_t = y_{t-\Delta}$, where Δ is the seasonality period. The Fourier series
309 serves as a natural foundation for modeling periodic functions:

$$\hat{y}_{s,l} = \sum_{i=0}^{\frac{H}{2}-1} \theta_{s,l,i}^f \cos(2\pi i t) + \theta_{s,l,i+[\frac{H}{2}]}^f \sin(2\pi i t) \quad (\text{Equation 12})$$

310

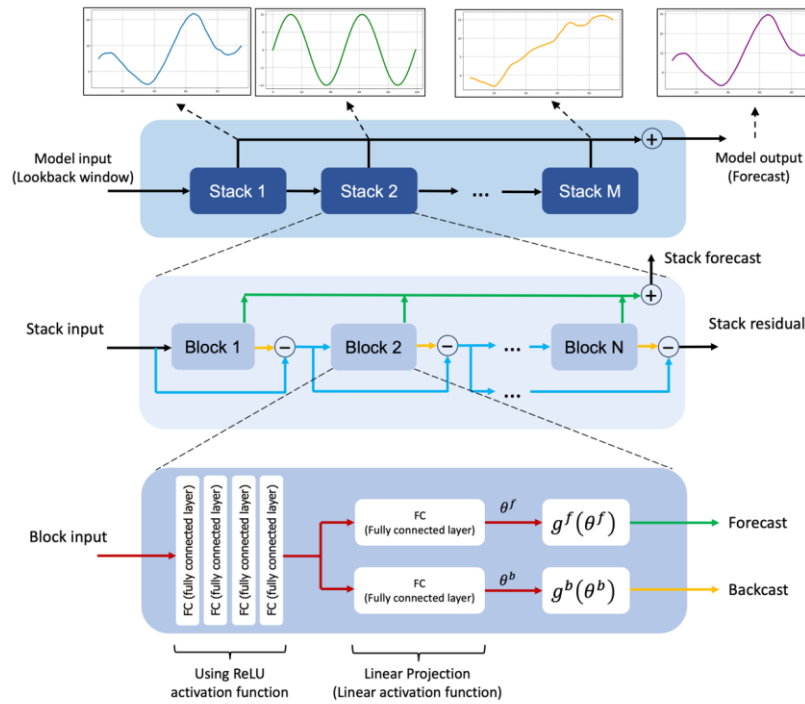
311 Consequently, the seasonality forecast is represented in the following matrix form:

$$\hat{y}_{s,l}^{seas} = S \theta_{s,l}^f \quad (\text{Equation 13})$$

$$S = [1, \cos(2\pi t), \dots, \cos\left(2\pi \left[\frac{H}{2}-1\right] t\right), \sin(2\pi t), \dots, \sin\left(2\pi \left[\frac{H}{2}-1\right] t\right)] \quad (\text{Equation 14})$$

312

313 Where the Fourier coefficients $\theta_{s,l}^f$, that predicted by an FC network at layer l of stack s , are described by
314 Equations (6) and (7). The matrix S represents sinusoidal waveforms. As a result, the forecast $\hat{y}_{s,l}^{seas}$
315 becomes a periodic function that imitates typical seasonal patterns (Oreshkin et al., 2020).



316

317

Figure 3. The N-BEATS modeling structure used in this research.

318 **2.2.3. N-HiTS**

319 N-HiTS builds upon the N-BEATS architecture but with improved accuracy and computational efficiency
 320 for long-horizon forecasting. N-HiTS utilizes multi-rate sampling and multi-scale synthesis of forecasts,
 321 leading to a hierarchical forecast structure that lowers computational demands and improves prediction
 322 accuracy (Challu et al., 2022).

323 Like N-BEATS, N-HiTS employs local nonlinear mappings onto foundational functions within numerous
 324 blocks. Each block includes an MLP that generates backcast and forecast output coefficients. The backcast
 325 output refines the input data for the following blocks, and the forecast outputs are combined to generate the
 326 final prediction. Blocks are organized into stacks, with each stack dedicated to grasping specific data
 327 attributes using its own distinct set of functions. The network's input is a sequence of L lags (look-back
 328 period), with S stacks, each containing B blocks (Challu et al., 2022).

329 In each block, a *MaxPool* layer with varying kernel sizes (k_l) is employed at the input, enabling the block
 330 to focus on specific input components of different scales. Larger kernel sizes emphasize the analysis of
 331 larger-scale, low-frequency data, aiding in improving long-term forecasting accuracy. This approach,
 332 known as multi-rate signal sampling, alters the effective input signal sampling rate for each block's MLP
 333 (Challu et al., 2022).

334 Additionally, multi-rate processing has several advantages. It reduces memory usage, computational
 335 demands, the number of learnable parameters, and helps prevent overfitting, while preserving the original
 336 receptive field. The following operation is applicable to the input $y_{t-L:t,l}$ of each block, with the first block
 337 ($l = 1$) using the network-wide input, where $y_{t-L:t,1} \equiv y_{t-L:t}$.

$$y_{t-L:t,l} = \text{MaxPool} (y_{t-L:t,l}, k_l) \quad (\text{Equation 15})$$

338 In many multi-horizon forecasting models, the number of neural network predictions matches the horizon's
 339 dimensionality, denoted as H . For instance, in N-BEATS, the number of predictions $|\theta_l^f| = H$. This results
 340 in a significant increase in computational demands and an unnecessary surge in model complexity as the
 341 horizon H becomes larger (Challu et al., 2022).

342 To address these challenges, N-HiTS proposes the use of temporal interpolation. This model manages the
 343 parameter counts per unit of output time ($|\theta_l^f| = [r_l H]$) by defining the dimensionality of the interpolation
 344 coefficients with respect to the expressiveness ratio r_l . To revert to the original sampling rate and predict
 345 all horizon points, this model employs temporal interpolation through the function g :

$$\hat{y}_{\tau,l} = g(\tau, \theta_l^f), \quad \forall \tau \in \{t + 1, \dots, t + H\}, \quad (\text{Equation 16})$$

$$\tilde{y}_{\tau,l} = g(\tau, \theta_l^b), \quad \forall \tau \in \{t - L, \dots, t\}, \quad (\text{Equation 17})$$

$$g(\tau, \theta) = \theta[t_1] + \left(\frac{\theta[t_2] - \theta[t_1]}{t_2 - t_1} \right) (\tau - t_1) \quad (\text{Equation 18})$$

$$t_1 = \arg \min_{t \in \tau: t \leq \tau} \tau - t, \quad t_2 = t_1 + 1/r_l \quad (\text{Equation 19})$$

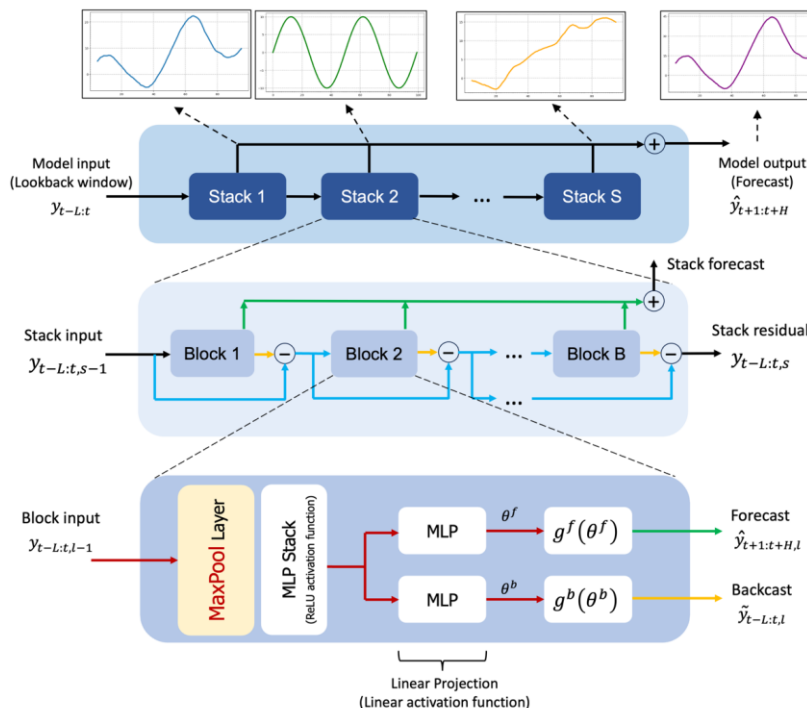
346 The hierarchical interpolation approach involves distributing expressiveness ratios over blocks, integrated
 347 with multi-rate sampling. Blocks closer to the input employ more aggressive interpolation, generating lower
 348 granularity signals. These blocks specialize in analyzing more aggressively subsampled signals. The final
 349 hierarchical prediction, $\hat{y}_{t+1:t+H}$, is constructed by combining outputs from all blocks, creating

350 interpolations at various time-scale hierarchy levels. This approach maintains a structured hierarchy of
 351 interpolation granularity, with each block focusing on its own input and output scales (Challu et al., 2022).

352 To manage a diverse set of frequency bands while maintaining control over the number of parameters,
 353 exponentially increasing expressiveness ratios are recommended. As an alternative, each stack can be
 354 dedicated to modeling various recognizable cycles within the time series (e.g., weekly, or daily) employing
 355 matching r_l . Ultimately, the residual obtained from backcasting in the preceding hierarchy level is
 356 subtracted from the input of the subsequent level, intensifying the next-level block's attention on signals
 357 outside the previously addressed band (Challu et al., 2022).

$$\hat{y}_{t+1:t+H} = \sum_{l=1}^L \hat{y}_{t+1:t+H,l} \quad (\text{Equation 20})$$

$$y_{t-L:t,l+1} = y_{t-L:t,l} - \tilde{y}_{t-L:t,l} \quad (\text{Equation 21})$$



359 Figure 4. The structure of N-HiTS model programmed in this study. The architecture includes several
360 Stacks, each Stack includes several Block, where each block consists of a MaxPool layer and a multi-
361 layer which learn to produce coefficients for the backcast and forecast outputs of its basis.

362 **2.3. Performance Metrics**

363 To comprehensively evaluate the accuracy of flood predictions, we utilized a suite of metrics, including
364 Nash-Sutcliffe Efficiency (NSE; Nash and Sutcliffe, 1970), persistent Nash-Sutcliffe Efficiency (persistent-
365 NSE), Kling–Gupta efficiency (KGE; Gupta et al. 2009), Root Mean Square Error (RMSE), Mean
366 Absolute Error (MAE), Peak Flow Error (PFE), and Time to Peak Error (TPE; Evin et al., 2023; Lobjigeois
367 et al., 2014). These metrics collectively facilitate a rigorous assessment of the model's performance in
368 reproducing the magnitude of observed peak flows and the shape of the hydrograph.

369 NSE measures the model's ability to explain the variance in observed data and assesses the goodness-of-fit
370 by comparing the observed and simulated hydrographs. In hydrological studies, the NSE index is a widely
371 accepted measure for evaluating the fitting quality of models (McCuen et al., 2006). It is calculated as:

$$NSE = 1 - \frac{\sum_{i=1}^n (Q_{s_i} - Q_{o_i})^2}{\sum_{i=1}^n (Q_{o_i} - \bar{Q}_o)^2} \quad (\text{Equation 22})$$

372 Where Q_{o_i} represents observed value at time i , Q_{s_i} represents simulated value at time i , \bar{Q}_o is the mean
373 observed values and n is the number of data points. An NSE value of 1 indicates a perfect match between
374 the observed and modeled data, while lower values represent the degree of departure from a perfect fit.

375 As the models are designed to predict one hour ahead [in one of the prediction horizons](#), the persistent-NSE
376 is essential for evaluating their performance. The standard NSE measures the model's sum of squared errors
377 relative to the sum of squared errors when the mean observation is used as the forecast value. In contrast,
378 persistent-NSE uses the most recent observed data as the forecast value for comparison (Nevo et al., 2022).
379 The persistent-NSE is calculated as:

$$persistent - NSE = 1 - \frac{\sum_{i=1}^n (Q_{s_i} - Q_{o_i})^2}{\sum_{i=1}^n (Q_{o_i} - Q_{o_{i-1}})^2} \quad (\text{Equation 23})$$

380 Where Q_{o_i} represents the observed value at time i , Q_{s_i} represents the simulated value at time i , $Q_{o_{i-1}}$ is the
381 observed value at the last time step ($i - 1$) and n is the number of data points.

382 The KGE is a widely used performance metric in hydrological modeling and combines multiple aspects of
383 model performance, including correlation, variability bias, and mean bias. The KGE metric is calculated
384 using the following equation:

$$KGE = 1 - \sqrt{(r - 1)^2 + (\alpha - 1)^2 + (\beta - 1)^2} \quad (\text{Equation 24})$$

385 Where r represents Pearson correlation coefficient between observed Q_o and simulated Q_s values.
386 α represents bias ratio, calculated as $\alpha = \frac{\mu_s}{\mu_o}$ where μ_s and μ_o are the means of simulated and observed data,
387 respectively. β represents variability ratio, calculated as $\beta = \frac{\sigma_s/\mu_s}{\sigma_o/\mu_o}$ where σ_s and σ_o are the standard
388 deviations of simulated and observed data, respectively.

389 RMSE quantifies the average magnitude of errors between observed and modeled values, offering insights
390 into the absolute goodness-of-fit, while MAE is a measure of the average absolute difference between the
391 modeled values and the observed values and provides a measure of the average magnitude of errors. RMSE
392 is calculated as:

$$RMSE = \sqrt{\frac{1}{n} \sum_{i=1}^n (Q_{o_i} - Q_{s_i})^2} \quad (\text{Equation 25})$$

393 and MAE is calculated as:

$$MAE = \frac{1}{n} \sum_{i=1}^n |Q_{o_i} - Q_{s_i}| \quad (\text{Equation 26})$$

394 Where Q_{o_i} represents observed value at time i , Q_{s_i} represents simulated value at time i , and n is the number
395 of data points. RMSE and MAE provide information about the magnitude of modeling errors, with smaller
396 values indicating a better model fit.

397 PFE quantifies the magnitude disparity between observed and modeled peak flow values. The PFE metric
398 is defined as:

$$PFE = \frac{|Q_{o_{max}} - Q_{s_{max}}|}{Q_{o_{max}}} \quad (\text{Equation 27})$$

399 Where $Q_{o_{max}}$ represents the observed peak flow value, and $Q_{s_{max}}$ signifies the simulated peak flow value.
400 The PFE metric, expressed as a dimensionless value, provides a quantitative measure of the relative error
401 in predicting peak flow magnitudes concerning the observed values. A smaller PFE denotes more accurate
402 modeling of peak flow magnitudes, with a value of zero indicating a perfect match.

403 TPE assesses the temporal alignment of peak flows in the observed and modeled hydrographs. The TPE
404 metric is computed as:

$$TPE = |T_{o_{max}} - T_{s_{max}}| \quad (\text{Equation 28})$$

405 Where $T_{o_{max}}$ signifies the time at which the peak flow occurs in the observed hydrograph, and $T_{s_{max}}$
406 represents the time at which the peak flow occurs in the simulated hydrograph. TPE that is measured in
407 units of time (hours), provides insight into the precision of peak flow timing. Smaller TPE values indicate
408 a superior alignment between the observed and modeled peak flow timing, while larger TPE values indicate
409 discrepancies in the temporal occurrence of peak flows.

410 The utilization of these five metrics, PFE, persistent-NSE, TPE, NSE, and RMSE, collectively provides a
411 robust and multifaceted assessment of flood prediction performance. This approach ensures that both the
412 magnitude and timing of peak flows, as well as the overall hydrograph shape, are accurately calibrated and
413 validated.

414 2.4. Sensitivity and Uncertainty Analysis

415 When implementing NN models, it's crucial to understand how each [input parameter feature](#) affects the
416 model's performance or outputs. To achieve this, we systematically excluded each [input feature parameter](#)
417 from the model one by one (the Leave-One-Out method). For each exclusion, we retrained the model
418 without that specific [input feature parameter](#) and then tested its performance against a test dataset. This
419 method helps in understanding which [input features parameters](#) are most critical to the model's performance
420 and which ones have a lesser impact. It also allows us to identify any [input features parameters](#) that may be
421 redundant or have little effect on the overall outcome, thus potentially simplifying the model without
422 sacrificing accuracy.

423 In this study, we utilized probabilistic approaches to quantify the uncertainty in flood prediction. This
424 method is rooted in statistical techniques employed for the estimation of unknown probability distributions,
425 with a foundation in observed data. More specifically, we leveraged the Maximum Likelihood Estimation
426 (MLE) approach, which entails the determination of [MLE parameter objective](#) values that optimize the

427 likelihood function. The likelihood function quantifies the probability of [MQL parameters-objective](#) taking
428 particular values, given the observed realizations.

429 We incorporated the MQL as a probabilistic error metric into the algorithmic architecture. MQL performs
430 an evaluation by computing the average loss for a predefined set of quantiles. This computation is grounded
431 in the absolute disparities between predicted quantiles and their corresponding observed values. By
432 considering multiple quantile levels, MQL provides a comprehensive assessment of the model's ability to
433 capture the distribution of the target variable, rather than focusing solely on point estimates.

434 The MQL metric also aligns closely with the Continuous Ranked Probability Score (CRPS), a standard tool
435 for evaluating predictive distributions. CRPS measures the difference between the predicted cumulative
436 distribution function and the observed values by integrating over all possible quantiles. The computation of
437 CRPS involves a numerical integration technique that discretizes quantiles and applies a left Riemann
438 approximation for CRPS integral computation. This process culminates in the averaging of these
439 computations over uniformly spaced quantiles, providing a robust evaluation of the predictive distribution
440 \hat{F}_t .

441 To calculate the 95th PPU, we utilized the 0.95 quantile level within the MQL. This quantile level directly
442 corresponds to the 95th percentile of the predicted distribution, providing an estimate of the 95% confidence
443 interval. By examining the model's performance at this specific quantile, we effectively assessed its ability
444 to accurately capture the predicted values with 95% confidence.

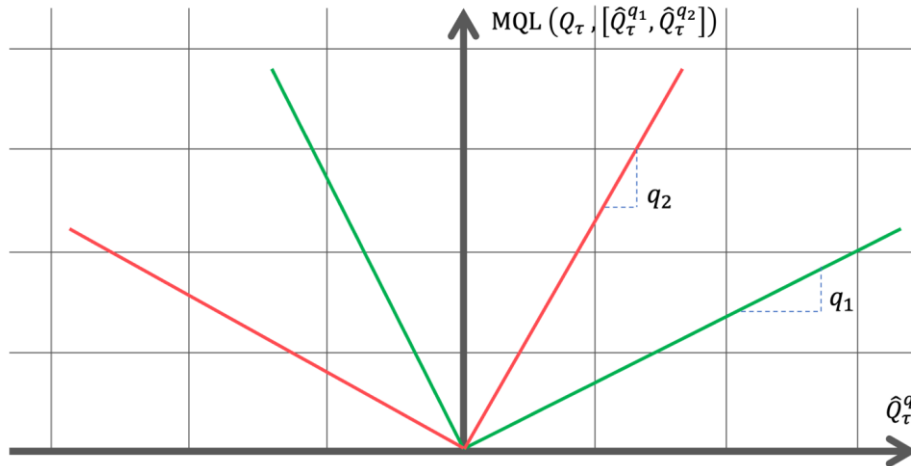
445 Incorporating MQL as a central metric in our study underscores its suitability for probabilistic forecasting,
446 particularly in the context of uncertainty quantification. Unlike traditional error metrics that focus on point
447 predictions, MQL captures both central tendencies and variability by penalizing errors symmetrically across
448 quantiles. This property ensures balanced and reliable assessments of the predictive distribution, ultimately
449 enhancing the robustness and interpretability of flood prediction models.

$$\text{MQL} (Q_\tau, [\hat{Q}_\tau^{q_1}, \dots, \hat{Q}_\tau^{q_i}]) = \frac{1}{n} \sum_{q_i} \text{QL} (Q_\tau, \hat{Q}_\tau^{q_i}) \quad (\text{Equation 29})$$

$$\text{CRPS} (Q_\tau, \hat{F}_\tau) = \int_0^1 \text{QL} (Q_\tau, \hat{Q}_\tau^{q_i}) dq \quad (\text{Equation 30})$$

$$\text{QL} (Q_\tau, \hat{Q}_\tau^q) = \frac{1}{H} \sum_{\tau=t+1}^{t+H} ((1-q)(\hat{Q}_\tau^q - Q_\tau) + q(Q_\tau - \hat{Q}_\tau^q)) \quad (\text{Equation 31})$$

450 Where Q_τ represents observed value at time τ , \hat{Q}_τ^q represents simulated value at time τ , q is the slope of the
 451 quantile loss, and H is the horizon of forecasting.



452
 453 Figure 5. The MQL function which shows loss values for different [parameters values](#) of q when the true
 454 value is Q_τ .

455 Furthermore, we employed two key indices, the R-Factor and the P-Factor, to rigorously assess the
 456 quality of uncertainty performance in our hydrological modeling. These metrics are instrumental in
 457 quantifying the extent to which the model's predictions encompass the observed data, thereby providing
 458 valuable insights into the model's predictive accuracy and reliability.

459 The P-Factor, or percentage of data within a 95PPU, is the first index used in this assessment. The P-Factor
 460 quantifies the percentage of observed data that falls within the 95PPU, providing a measure of the model's
 461 predictive accuracy. The P-Factor can theoretically vary from 0% to a maximum of 100%. A P-Factor of
 462 100% signifies a perfect alignment between the model's predictions and the observed data within the
 463 uncertainty band. In contrast, a lower P-Factor indicates a reduced ability of the model to predict data within
 464 the specified uncertainty range.

$$P - Factor = \frac{\text{Observations bracketed by 95PPU}}{\text{Number of observations}} \times 100 \quad (\text{Equation 32})$$

465 The R-Factor can be computed by dividing the average width of the uncertainty band by the standard
 466 deviation of the measured variable. The R-Factor, with a minimum possible value of zero, provides a
 467 measure of the spread of the uncertainty relative to the variability of the observed data. Theoretically, the

468 R-Factor spans from 0 to infinity, and a value of zero implies that the model's predictions precisely match
469 the measured data, with the uncertainty band being very narrow in relation to the variability of the observed
470 data.

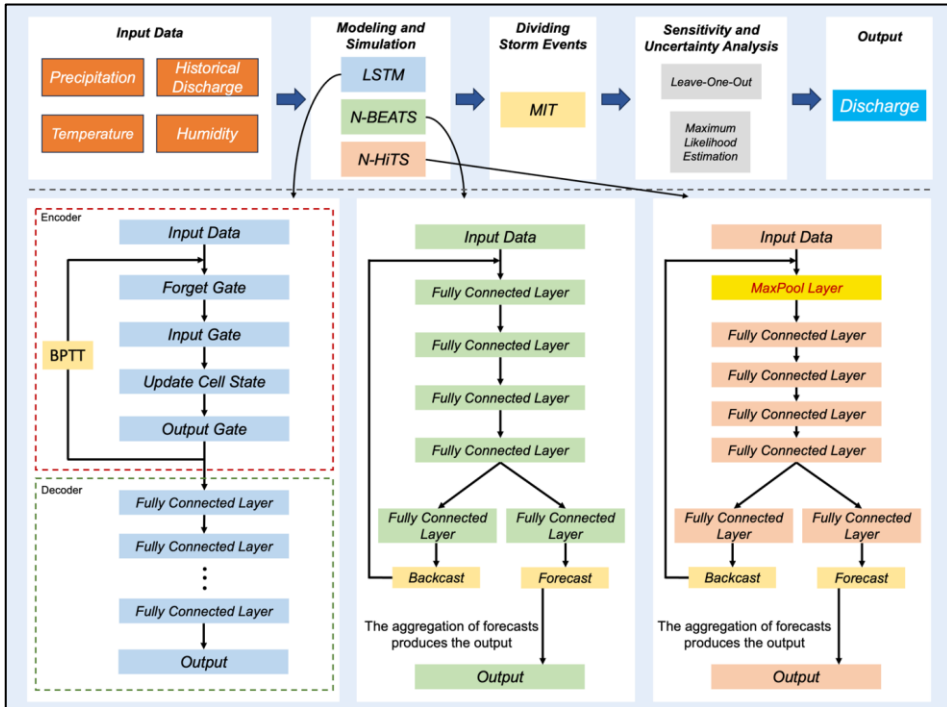
$$R - Factor = \frac{\text{Average width of 95PPU band}}{\text{Standard deviation of measured variables}} \times 100 \quad (\text{Equation 33})$$

471 In practice, the quality of the model is assessed by considering the 95% prediction band with the highest P-
472 Factor and the lowest R-Factor. This specific band encompasses the majority of observed records,
473 signifying the model's ability to provide accurate and reliable predictions while effectively quantifying
474 uncertainty. A simulation with a P-Factor of 1 and an R-Factor of 0 signifies an ideal scenario where the
475 model precisely matches the measured data within the uncertainty band (Abbaspour et al., 2007).

476 Figure 6 shows the workflow of programming N-BEATS, N-HiTS, and LSTM for flood prediction. As
477 illustrated, the initial step involved cleaning and preparing the input data, which was then used to feed the
478 models. The workflow for each model and their output generation processes are depicted in Figure 6. We
479 segmented the storm events using the MIT approach, as previously described. Following this, we conducted
480 a sensitivity analysis using the Leave-One-Out method and performed uncertainty analysis using the MLE
481 approach to construct the 95PPU band. This rigorous methodology ensures a robust evaluation of model
482 performance under varying conditions and highlights the models' predictive reliability and resilience. We
483 employed the "NeuralForecast" Python package to develop the N-BEATS, N-HiTS, and LSTM models.
484 This package provides a diverse array of NN models with an emphasis on usability and robustness.

485

486



487

Figure 6. The workflow of N-BEATS, N-HiTS, and LSTM implementation. The upper section of the figure illustrates multiple steps from data preprocessing to model evaluation. The lower section provides a detailed view of the workflow and implementation for each model, highlighting the specific processes and methodologies employed in generating the outputs. Backpropagation Through Time (BPTT) trains LSTM by unrolling the model through time, computing gradients for each time step, and updating weights based on temporal dependencies.

494 3. Results and Discussion

495 3.1. Independent Storms Delineation

496 MIT's contextual delineation of storm events laid the groundwork for in-depth evaluation of rainfall events,
497 enabling isolation and separation of rainfall events that led to significant flooding events. The nuanced
498 outcomes of the MIT assessment contributed significantly to the understanding of rainfall variability and
499 distribution as the dominant contributor to flood generation.

500 During modeling implementation, the initial imperative was the precise distinction of storm events within
501 the precipitation time series data of each case study. Our findings demonstrate that on average a dry period
502 of 7 hours serves as the optimal MIT time for both of our case studies. This outcome signifies that when a
503 dry interval of more than 7 hours transpires between two successive rainfall events, these subsequent
504 rainfalls should be considered two distinct storm events. This determination underlines the temporal
505 threshold necessary for distinguishing between individual meteorological phenomena in two case studies.

506 3.2. Hyperparameter Optimization

507 In the context of hyperparameter optimization, we systematically considered and tuned various
508 hyperparameters for the N-HiTS, N-BEATS, and LSTM. For all models, we searched searched for learning
509 rates on a log-uniform grid between 1×10^{-4} and 1×10^{-3} , batch sizes {16, 32, 64}, input size {1, 6, 12,
510 24}, hours. For the LSTM, we varied recurrent layers {1,2,3}, hidden units per layer {64,128,256},
511 activation {tanh, ReLU}, decoder MLP depth {1,2,3}, and decoder MLP width {64,128,256}. For N-HiTS,
512 we explored stacks {2,3,4}, blocks per stack {2,3,4,5}, block MLP width {64,128,256}, and block MLP
513 depth {2,3,4}. For N-BEATS, we searched stacks {2,3,4}, blocks per stack {2,3,4,5}, block MLP width
514 {64,128,256}, and block MLP depth {2,3,4}; the interpretable (trend/seasonality) basis was kept fixed.

515 Following extensive exploration and fine-tuning of these hyperparameters, the optimal configurations were
516 identified (see Table 2). For the N-HiTS model, the most favorable outcomes were achieved with the
517 following hyperparameter settings: 2000 epochs, "identity" for scalar type, a learning rate of 0.001, a batch
518 size of 32, input size of 24 hours, "identity" for stack type, 512 units for hidden layers of each stack, step
519 size of 1, MQLoss as loss function, and "ReLU" for the activation function. As shown in Table 2, the N-
520 HiTS model demonstrated superior performance with 4 stacks, containing 2 blocks each, and corresponding
521 coefficients of 48, 24, 12, and 1, showcasing the significance of these settings for flood prediction.

522 This hyperparameter optimization was also conducted for the N-BEATS model. In this model, we
523 considered 2000 epochs, 3 stacks with 2 blocks, "identity" for scalar type, a learning rate of 0.001, a batch
524 size of 32, input size of 24 hours, "identity" for stack type, 512 units for hidden layers of each stack, step
525 size of 1, MQLoss as loss function, and "ReLU" for the activation function.

526 Moreover, the LSTM as a benchmark model yielded its best results with 5000 epochs, an input size of 24
527 hours, "identity" as the scalar type, a learning rate of 0.001, a batch size of 32, and "tanh" as the activation
528 function. Furthermore, the LSTM's hidden state was most effective with two layers containing 128 units,
529 and the MLP decoder thrived with two layers encompassing 128 units. These meticulously optimized

- Formatted:** Font: (Default) +Headings CS (Times New Roman), 11 pt, Font color: Auto
- Formatted:** Font: (Default) +Headings CS (Times New Roman), 11 pt, Font color: Auto
- Formatted:** Font: (Default) +Headings CS (Times New Roman), 11 pt, Font color: Auto
- Formatted:** Font: 11 pt, Font color: Auto
- Formatted:** Font: 11 pt, Font color: Auto
- Formatted:** Font: (Default) +Headings CS (Times New Roman), 11 pt, Font color: Auto
- Formatted:** Font: (Default) +Headings CS (Times New Roman), 11 pt, Font color: Auto
- Formatted:** Font: (Default) +Headings CS (Times New Roman), 11 pt, Font color: Auto

530 hyperparameter settings represent the culmination of efforts to ensure that each model operates at its peak
531 potential, facilitating accurate flood prediction.

532 Table 2. Optimized values for the hyperparameters.

Hyperparameter	N-HiTS	N-BEATS	LSTM
Epoch	2000	2000	5000
Scaler type	identity	identity	standard
Learning rate	0.001	0.001	0.001
Batch size	32	32	32
Input size	24 hours	24 hours	24 hours
Stack type	Seasonality, trend, identity, identity	Seasonality, trend, identity	*
Number of units in each hidden layer	512	512	128
Loss function	MQLoss	MQLoss	MQLoss
Activation function	ReLU	ReLU	tanh
Number of stacks	4	3	*
Number of blocks in each stack	2	2	*
Stacks' coefficients	48,24,12,1	*	*

533 *Not applicable

534 In Table 2, "epoch" refers to the number of training steps, and "scaler type" indicates the type of scaler used
535 for normalizing temporal inputs. The "learning rate" specifies the step size at each iteration while optimizing
536 the model, and the "batch size" represents the number of samples processed in one forward and backward
537 pass. The "loss function" quantifies the difference between the predicted outputs and the actual target
538 values, while the "activation function" determines whether a neuron should be activated. The "stacks'
539 coefficients" in the N-HITS model control the frequency specialization for each stack, enabling effective
540 handling of different frequency components in the time series data.

541 Another hyperparameter for all three models is input size, which is a parameter variable that determines the
542 maximum sequence length for truncated backpropagation during training and the number of autoregressive
543 inputs (lags) that the models considered for prediction. Essentially, input size represents the length of the
544 historical series data used as input to the model. This parameter variable offers flexibility in the models,
545 allowing them to learn from a defined window of past observations, which can range from the entire

546 historical dataset to a subset, tailored to the specific requirements of the prediction task. In the context of
547 flood prediction, determining the appropriate input size is crucial to adequately capture the meteorological
548 data preceding the flood event. To address this, we calculated the time of concentration (*TC*) of the
549 watershed system and set the input size to exceed this duration. According to the Natural Resources
550 Conservation Service (NRCS), for typical natural watershed conditions, the *TC* can be calculated from lag
551 time, the time between peak rainfall and peak discharge, using the formula: $\text{Lag time} = \text{TC} \times 0.6$ (NRCS,
552 2009). Specifically, the average *TC* in the Lower Dog River watershed and Upper Dutchmans Creek
553 watershed was found to be 19 and 22 hours, respectively. As these represent the average *TC* for our case
554 studies, we selected the 24 hours for input data, slightly longer than the calculated average *TC*, ensuring
555 sufficient coverage of relevant meteorological data preceding all flood events.

556 **3.3. Flood Prediction and Performance Assessment**

557 In this study, we conducted a comprehensive performance evaluation of N-HiTS, N-BEATS, and
558 benchmarked these models with LSTM, utilizing two case studies: the Lower Dog River and the Upper
559 Dutchmans Creek watersheds. Within these case studies, we trained and validated the models separately
560 for each watershed across a diverse set of storm events from 01/10/2007 to 01/10/2022 (15 years) in the
561 Lower Dog River and from 21/12/1994 to 01/10/2022 (27 years) in the Upper Dutchmans Creek. The
562 decision to train separate models for each catchment was made to account for the unique hydrological
563 characteristics and local features specific to each watershed. By training models individually, we aimed to
564 optimize performance by tailoring each model to the distinct rainfall-runoff relationship inherent in each
565 catchment. All algorithms were tested using unseen flooding events that occurred between 14/12/2022 and
566 28/03/2023. Our targets were event-focused, where operational value focuses on performance during rising
567 limbs, peaks, and recessions. Evaluating over the entire continuous hydrograph (testing period) can dilute
568 or even mask differences. For this reason, we prioritized an event-centric assessment as the primary
569 evaluation approach rather than full-period metrics. For this reason, our primary assessment is event-centric
570 rather than full period. In the Dog River gauging station, two winter ~~storms~~storms, i.e., January 3rd to
571 January 5th, 2023 (Event 1) and February 17th to February 18th, 2023 (Event 2), as well as a spring flood
572 event that occurred during March 26th to March 28th, 2023 (Event 3) were selected for testing.
573 Additionally, three winter flooding events, i.e., December 14th to December 16th, 2022 (Event 4), January
574 25th and January 26th, 2023 (Event 5), and February 11th to February 13th, 2023 (Event 6), were chosen
575 to test the algorithms across the Killian Creek gauging station in the Upper Dutchmans Creek. The rainfall
576 events corresponding to these flooding events were delineated using the MIT technique discussed in Section
577 3.1.

Formatted: Font: 11 pt

Formatted: Font: Not Bold

578 Our results for the Lower Dog River case study, explicitly demonstrated the accuracy of both N-HiTS and
579 N-BEATS in generating the winter and spring flood hydrographs compared to the LSTM model across all
580 selected storm events. Although, N-HiTS prediction slightly outperformed N-BEATS during winter
581 prediction (January 3rd to January 5th, 2023). In this event, N-HiTS outperformed N-BEATS with a
582 difference of 11.6% in MAE and 20% in RMSE. The N-HiTS slight outperformance (see Tables 3 and 4)
583 is attributed to its unique structure that allows the model to discern and capture intricate patterns within the
584 data. Specifically, N-HiTS predicted flooding events hierarchically using blocks specialized in different
585 rainfall frequencies based on controlled signal projections, through expressiveness ratios, and interpolation
586 of each block. The coefficients are then used to synthesize backcast through
587 $\tilde{y}_t - L: t, l$ and forecast $(\tilde{y}_{t+1}: t + H, l)$ outputs of the block as a flood value. The coefficients were locally
588 determined along the horizon, allowing N-HiTS to reconstruct nonstationary signals over time.

589 While the N-HiTS emerged as the most accurate in predicting flood hydrograph among the three models,
590 its performance was somehow comparable with N-BEATS. The N-BEATS model exhibited good
591 performance in two case studies. It consistently provided competitive results, demonstrating its capacity to
592 effectively handle diverse storm events and deliver reliable predictions. N-BEATS has a generic and
593 interpretable architecture depending on the blocks it uses. Interpretable configuration sequentially projects
594 the signal into polynomials and harmonic basis to learn trend and seasonality components while generic
595 configuration substitutes the polynomial and harmonic basis for identity basis and larger network's depth.
596 In this study, we used interpretable architecture, as it regularizes its predictions through projections into
597 harmonic and trend basis that is well-suited for flood prediction tasks. Using interpretable architecture,
598 flood prediction was aggregated in a hierarchical fashion. This enabled the building of a very deep neural
599 network with interpretable flood prediction outputs.

600 It is essential to underscore that, despite its strong performance, the N-BEATS model did not surpass the
601 N-HiTS model in terms of NSE, Persistent-NSE, MAE, and RMSE for the Lower Dog River case study.
602 Although both models showed almost the same KGE values. Notably, the N-BEATS model showcased
603 superior results based on the PFE metric, signifying its exceptional capability in accurately predicting flood
604 peaks. However, both N-HiTS and N-BEATS models overestimated the flood peak rate of Event 2 for the
605 Lower Dog River watershed. This event, which occurred from February 17th to February 18th, 2023, was
606 flashy, short, and intense proceeded by a prior small rainfall event (from February 12th until February 13th)
607 that minimized the rate of infiltration. This flash flood event caused by excessive rainfall in a short period
608 of time (<8 hours) was challenging to predict for N-BEATS and N-HiTS models. In addition, predicting
609 the magnitude of changes in the recession curve of the third event seems to be a challenge for both models.
610 The specific part of the flood hydrograph after the precipitation event, where flood diminishes during a

rainless is dominated by the release of runoff from shallow aquifer systems or natural storages. It seems both models showed a slight deficiency in capturing this portion of the hydrograph when the rainfall amount decreases over time in the Dog River gauging station.

Conversely, in the Killian Creek gauging station, the N-BEATS model almost emerged as the top performer in predicting the flood hydrograph based on NSE, Persistent-NSE, RMSE, and PFE performance metrics (see Tables 3 and 4). KGE values remained almost the same for both models. In addition, both N-BEATS and N-HiTS slightly overpredicted time to peak values for Event 5. This reflects the fact that when rainfall value varies randomly around zero, it provides less to no information for the algorithms to learn the fluctuations and patterns in time series data. Both N-HiTS and N-BEATS provided comparable results for all events predicted in this study. N-HiTS builds upon N-BEATS by adding a MaxPool layer at each block. Each block consists of an MLP layer that learns to produce coefficients for the backcast and forecast outputs. This subsamples the time series and allows each stack to focus on either short-term or long-term effects, depending on the pooling kernel size. Then, the partial predictions of each stack are combined using hierarchical interpolation. This ability enhances N-HiTS capabilities to produce drastically improved, interpretable, and computationally efficient long-horizon flood predictions.

In contrast, the performance of LSTM as a benchmark model lagged behind both N-HiTS and N-BEATS models for all events across two case studies. Despite its extensive applications in various hydrology domains, the LSTM model exhibited comparatively lower accuracy when tasked with predicting flood responses during different storm events. Focusing on NSE, Persistent-NSE, KGE, MAE, RMSE, and PFE metrics, it is noteworthy that all three models, across both case studies, consistently succeeded in capturing peak flow rates at the appropriate timing. All models demonstrated commendable results with respect to the TPE metric. In most scenarios, TPE revealed a value of 0, signifying that the models accurately pinpointed the peak flow rate precisely at the expected time. In some instances, TPE reached a value of 1, showing a deviation of one hour in predicting the peak flow time. This deviation is deemed acceptable, particularly considering the utilization of short, intense rainfall for our analysis.

Our investigation into the performance of the three distinct forecasting models yielded compelling results pertaining to their ability to generate 95PPU, as quantified by the P-Factor and R-Factor. These factors serve as critical indicators for assessing the reliability and precision of the uncertainty bands produced by the MLE. Our findings demonstrated that the N-HiTS and N-BEATS models outperformed the LSTM model in mathematically defining uncertainty bands, in terms of R-Factor metric. The R-Factor, a crucial metric for evaluating the average width of the uncertainty band, consistently favored the N-HiTS and N-BEATS models over their counterparts. This finding was consistent across a diverse range of storm events.

643 In addition, coupling MLE with the N-HiTS and N-BEATS models demonstrated superior performance in
644 generating 95PPU when assessed through the P-Factor metric. The P-Factor represents another vital aspect
645 of uncertainty quantification, focusing on the precision of the uncertainty bands.

646 Figures 8-7 and 9-8 present graphical depictions of the predicted flood with [1-hour prediction horizon and](#)
647 uncertainty assessment for each model as well as Flow Duration Curve (FDC) across two gauging
648 stations. As illustrated, the uncertainty bands skillfully bracketed most of the observational data, reflecting
649 the fact that MLE was successful in reducing errors in flood prediction. FDC analysis also revealed that N-
650 HiTS and N-BEATS models skillfully predicted the flood hydrograph, however, both models were
651 particularly successful in predicting moderate to high flood events (1800-6000 and >6000 cfs). In the FDC
652 plots, the x-axis denotes the exceedance probability, expressed as a percentage, while the y-axis signifies
653 flood in cubic feet per second. Notably, these plots reveal distinctive patterns in the performance of the N-
654 HiTS, N-BEATS, and LSTM models. Within the lower exceedance probability range, particularly around
655 the peak flow, the N-HiTS and N-BEATS models demonstrated a clear superiority over the LSTM model,
656 closely aligning with the observed data. This observed trend is consistent when examining the
657 corresponding hydrographs. Across all events, the flood hydrographs generated by N-HiTS and N-BEATS
658 exhibited a closer resemblance to the observed data, particularly in the vicinity of the peak timing and rate,
659 compared to the hydrographs produced by the LSTM model. These findings underscore the enhanced
660 predictive accuracy and reliability of the N-HiTS and N-BEATS models, particularly in predicting
661 moderate to high flood events as well as critical hydrograph features such as peak flow rate and timing. The
662 alignment of model-generated FDCs and hydrographs with observed data in the proximity of peak flow
663 further establishes the efficiency of N-HiTS and N-BEATS in accurately reproducing the dynamics of flood
664 generation mechanisms across two headwater streams.

665
666 Table 3. The performance metrics for the Lower Dog River flood predictions [with 1-hour prediction](#)
667 [horizon.](#)

Model	Performance Metric	Event 1	Event 2	Event 3
N-HiTS	NSE	0.995	0.991	0.992
	Persistent-NSE	0.947	0.931	0.948
	KGE	0.977	0.989	0.976
	RMSE	123.2	27.6	68.5
	MAE	64.1	12.0	37.8
	PFE	0.018	0.051	0.015
TPE (hours)		0	1	0

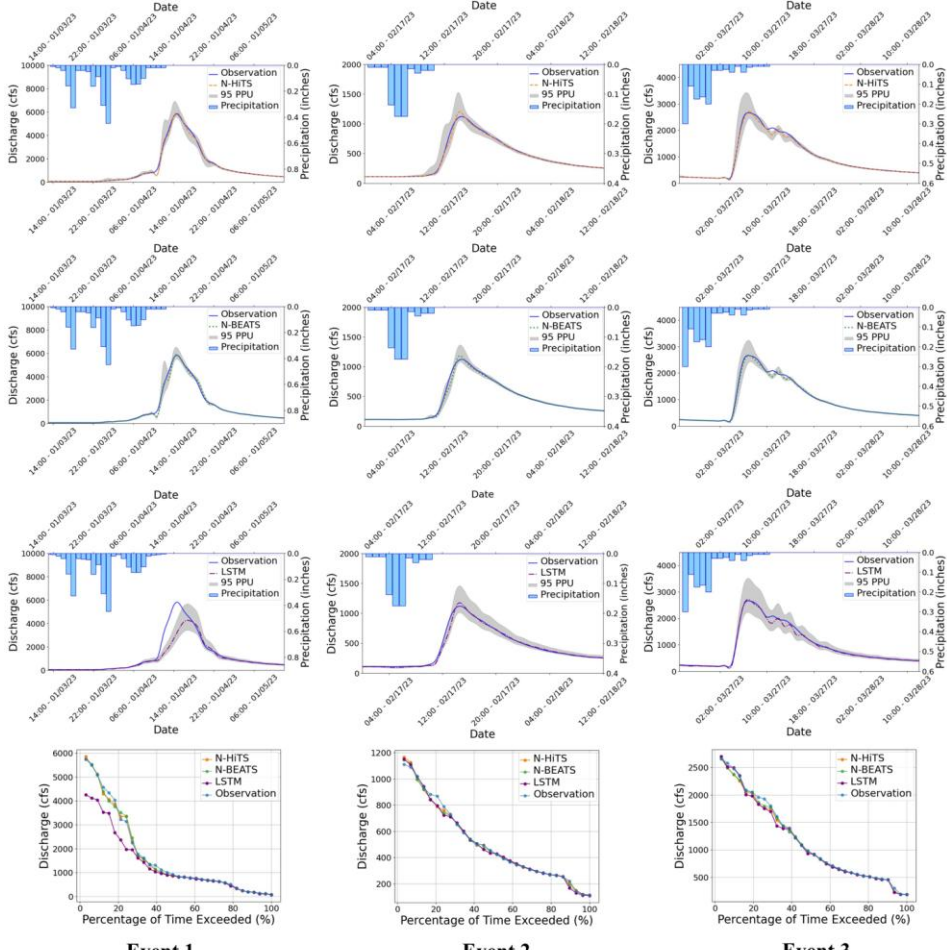
	P-Factor	96.9 %	100 %	93.5 %
	R-Factor	0.27	0.40	0.33
	NSE	0.991	0.989	0.993
	Persistent-NSE	0.917	0.916	0.956
	KGE	0.984	0.984	0.98
	RMSE	154.1	30.5	62.5
N-BEATS	MAE	72.6	13.6	35.9
	PFE	0.0005	0.031	0.0002
	TPE (hours)	0	1	0
	P-Factor	87.8 %	100 %	90.3 %
	R-Factor	0.17	0.23	0.24
	NSE	0.756	0.983	0.988
	Persistent-NSE	-1.44	0.871	0.929
	KGE	0.765	0.978	0.971
	RMSE	841.1	37.9	79.5
LSTM	MAE	369.4	18.6	42
	PFE	0.258	0.036	0.016
	TPE (hours)	1	0	0
	P-Factor	81.8 %	93.1 %	96.7 %
	R-Factor	0.37	0.51	0.6

668

669 Table 4. The performance metrics for the Killian Creek flood predictions [with 1-hour prediction horizon](#).

Model	Performance Metric	Event 4	Event 5	Event 6
	NSE	0.991	0.971	0.991
	Persistent-NSE	0.885	0.806	0.844
	KGE	0.982	0.967	0.991
	RMSE	28.8	46.0	19.0
N-HITS	MAE	17.9	23.8	11.5
	PFE	0.017	0.008	0.020
	TPE (hours)	0	0	0
	P-Factor	92.6 %	90.9 %	100 %
	R-Factor	0.39	0.48	0.45

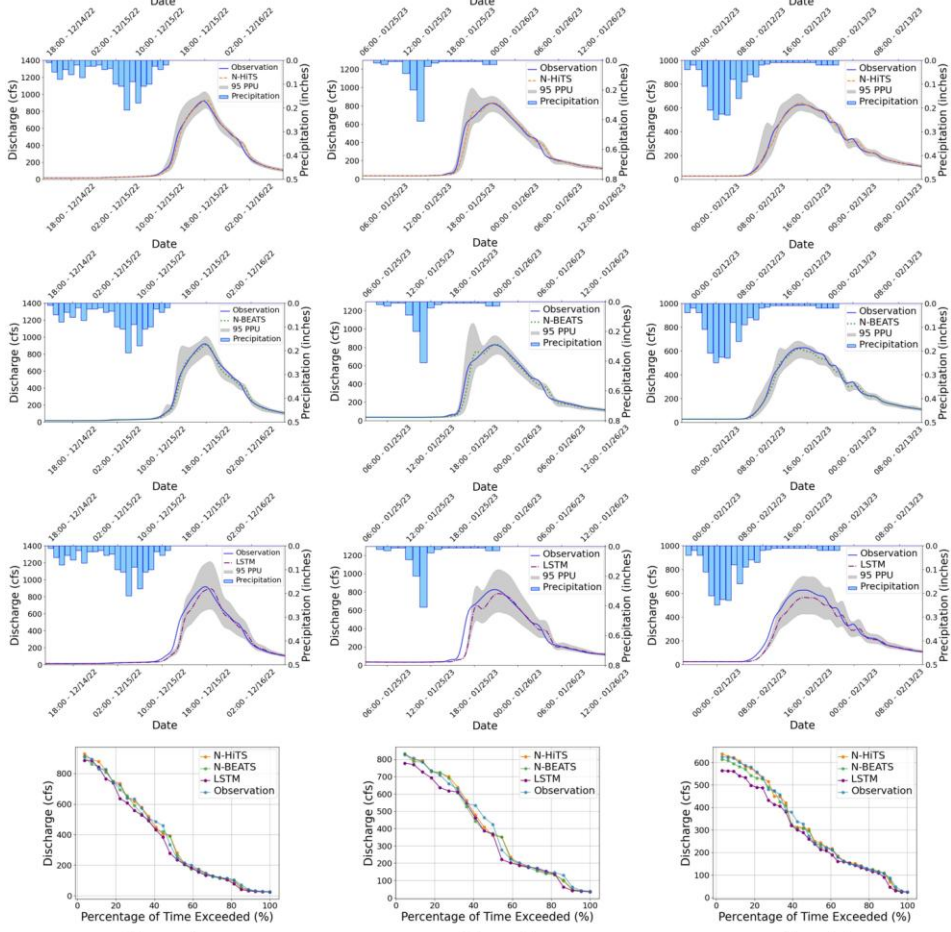
	NSE	0.992	0.973	0.989
	Persistent-NSE	0.908	0.821	0.823
	KGE	0.972	0.951	0.973
	RMSE	25.7	44.2	20.2
N-BEATS	MAE	18.3	25.9	14.0
	PFE	0.006	0.008	0.019
	TPE (hours)	0	0	0
	P-Factor	96.3 %	86.3 %	96.9 %
	R-Factor	0.43	0.53	0.43
	NSE	0.952	0.892	0.935
	Persistent-NSE	0.4	0.27	0.087
LSTM	KGE	0.92	0.899	0.901
	RMSE	65.7	89.2	50.3
	MAE	41.1	45	35.9
	PFE	0.031	0.058	0.098
	TPE (hours)	1	0	0
	P-Factor	70.4 %	72.73 %	81.82 %
	R-Factor	0.66	0.7	0.65



671

672
673

Figure 7. 95 PPU band and FDC plots of N-HiTS, N-BEATS, and LSTM models [with 1-hour prediction horizon](#) for the three selected flooding events in the Lower Dog River gauging station.



674
675 Figure 8. 95 PPU band and FDC plots of N-HiTS, N-BEATS, and LSTM models [with 1-hour prediction](#)
676 [horizon](#) for the three selected flooding events in the Killian Creek gauging station.

677 To evaluate robustness across lead times, we extended the analysis to 3- and 6-hour prediction horizons.
678 The results are presented in [Figures 9-12](#), and tables 5 and 6. As expected, NSE and KGE decreased, and
679 absolute errors increased with horizon for all models; however, N-HiTS and N-BEATS continued to
680 outperform LSTM across both stations and storm events. At Killian Creek station, both N-HiTS and N-
681 BEATS preserved their lead, yielding higher NSE and lower MAE/RMSE than LSTM, while at the Lower
682 Dog River, N-BEATS remained slightly superior on the same metrics. KGE values stayed comparable
683 between the two feed-forward models, and peak-focused metrics (PFE and TPE) indicated that both still

Formatted: Font: 11 pt

684 captured peak magnitude and timing reliably, compared to LSTM. Uncertainty bands widened with horizon
 685 as expected, but the likelihood-based 95PPU for N-HiTS and N-BEATS maintained tighter R-Factors and
 686 competitive P-Factors relative to LSTM, especially around moderate-to-high flows. Flow-duration
 687 diagnostics at multi-hour leads reinforced these findings, showing closer alignment of N-HiTS and N-
 688 BEATS to observations in the upper tail. Overall, the multi-horizon results corroborate the 1-hour horizon
 689 results: N-HiTS and N-BEATS deliver more accurate and reliable flood forecasts than LSTM, and their
 690 relative strengths persist at 3 and 6 hours ahead. For completeness, we also evaluated 12- and 24-hour lead
 691 times. All models' performances declined sharply (NSE < 0.4 across sites and events), so we
 692 restrict detailed reporting to 1–6 hours where performance remains operationally meaningful.

Formatted: Font: 11 pt

Table 5. The performance metrics of the models with 3-hour prediction horizon.

Model	Performance Metric	Event 1	Event 2	Event 3	Event 4	Event 5	Event 6
N-HiTS	<u>NSE</u>	0.91	0.86	0.58	0.83	0.81	0.89
	<u>KGE</u>	0.92	0.92	0.74	0.85	0.85	0.88
	<u>RMSE</u>	506	107	485	122	119	65
	<u>MAE</u>	293	58	209	71	65	42
	<u>PFE</u>	0.03	0.02	0.08	0.1	0.07	0.05
	<u>TPE (hours)</u>	0	0	0	0	0	0
	<u>P-Factor</u>	97 %	100 %	93.5 %	85 %	72 %	88 %
	<u>R-Factor</u>	0.8	1.3	0.75	0.99	0.92	1.14
N-BEATS	<u>NSE</u>	0.92	0.88	0.56	0.82	0.82	0.89
	<u>KGE</u>	0.91	0.91	0.72	0.83	0.84	0.87
	<u>RMSE</u>	481	101	498	124	115	63
	<u>MAE</u>	241	48	207	67	58	33
	<u>PFE</u>	0.04	0.02	0.12	0.006	0.02	0.002
	<u>TPE (hours)</u>	1	0	2	0	0	0
	<u>P-Factor</u>	90.9 %	93 %	90.3 %	92 %	68 %	94 %
	<u>R-Factor</u>	0.7	1.2	0.74	0.78	1.1	0.87
LSTM	<u>NSE</u>	0.7	0.77	0.42	0.82	0.51	0.55
	<u>KGE</u>	0.765	0.87	0.65	0.79	0.64	0.69
	<u>RMSE</u>	928	139	575	125	190	133
	<u>MAE</u>	487	80	296	85	118	87

Formatted Table

<u>PFE</u>	<u>0.12</u>	<u>0.03</u>	<u>0.16</u>	<u>0.16</u>	<u>0.44</u>	<u>0.08</u>
<u>TPE (hours)</u>	<u>2</u>	<u>1</u>	<u>2</u>	<u>2</u>	<u>1</u>	<u>2</u>
<u>P-Factor</u>	<u>75.8 %</u>	<u>96 %</u>	<u>83.9 %</u>	<u>100 %</u>	<u>90 %</u>	<u>94 %</u>
<u>R-Factor</u>	<u>1.15</u>	<u>1.88</u>	<u>1.66</u>	<u>2.8</u>	<u>3.7</u>	<u>2.4</u>

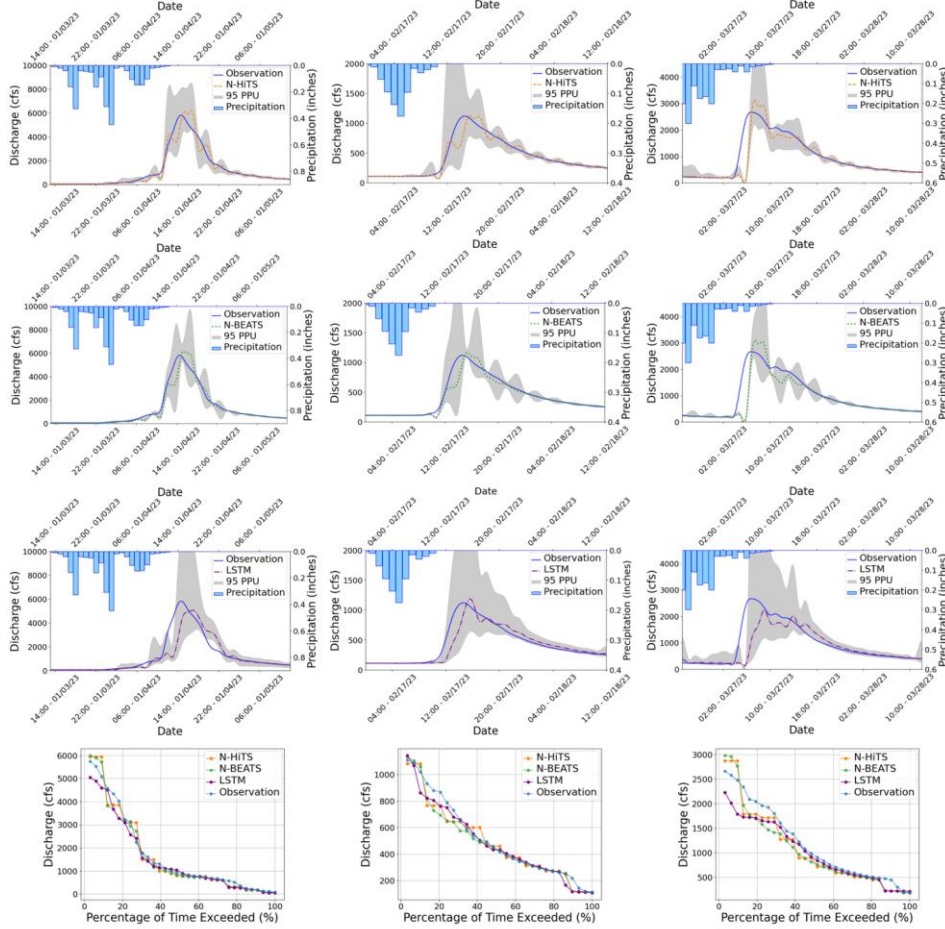
694

695

Table 6. The performance metrics of the models with 6-hour prediction horizon.

Model	Performance Metric	Event 1	Event 2	Event 3	Event 4	Event 5	Event 6
N-HiTS	<u>NSE</u>	<u>0.82</u>	<u>0.58</u>	<u>0.51</u>	<u>0.6</u>	<u>0.7</u>	<u>0.52</u>
	<u>KGE</u>	<u>0.76</u>	<u>0.68</u>	<u>0.67</u>	<u>0.74</u>	<u>0.78</u>	<u>0.67</u>
	<u>RMSE</u>	<u>708</u>	<u>189</u>	<u>525</u>	<u>188</u>	<u>147</u>	<u>137</u>
	<u>MAE</u>	<u>423</u>	<u>90</u>	<u>257</u>	<u>110</u>	<u>90</u>	<u>77</u>
	<u>PFE</u>	<u>0.35</u>	<u>0.29</u>	<u>0.12</u>	<u>0.03</u>	<u>0.2</u>	<u>0.1</u>
	<u>TPE (hours)</u>	<u>2</u>	<u>3</u>	<u>0</u>	<u>0</u>	<u>3</u>	<u>3</u>
	<u>P-Factor</u>	<u>70 %</u>	<u>96 %</u>	<u>87 %</u>	<u>92 %</u>	<u>82 %</u>	<u>87 %</u>
	<u>R-Factor</u>	<u>0.71</u>	<u>1.1</u>	<u>1.1</u>	<u>1.8</u>	<u>1.15</u>	<u>1.2</u>
	<u>TPE (hours)</u>	<u>2</u>	<u>3</u>	<u>0</u>	<u>0</u>	<u>3</u>	<u>3</u>
N-BEATS	<u>NSE</u>	<u>0.94</u>	<u>0.85</u>	<u>0.59</u>	<u>0.33</u>	<u>0.82</u>	<u>0.59</u>
	<u>KGE</u>	<u>0.83</u>	<u>0.82</u>	<u>0.73</u>	<u>0.55</u>	<u>0.79</u>	<u>0.67</u>
	<u>RMSE</u>	<u>386</u>	<u>112</u>	<u>481</u>	<u>244</u>	<u>115</u>	<u>126</u>
	<u>MAE</u>	<u>259</u>	<u>58</u>	<u>181</u>	<u>131</u>	<u>56</u>	<u>74</u>
	<u>PFE</u>	<u>0.16</u>	<u>0.23</u>	<u>0.02</u>	<u>0.03</u>	<u>0.03</u>	<u>0.12</u>
	<u>TPE (hours)</u>	<u>0</u>	<u>3</u>	<u>0</u>	<u>0</u>	<u>0</u>	<u>3</u>
	<u>P-Factor</u>	<u>100 %</u>	<u>86 %</u>	<u>90.3 %</u>	<u>85 %</u>	<u>77 %</u>	<u>78 %</u>
	<u>R-Factor</u>	<u>1.8</u>	<u>2.3</u>	<u>1.1</u>	<u>1.13</u>	<u>3.3</u>	<u>1.2</u>
	<u>TPE (hours)</u>	<u>0</u>	<u>3</u>	<u>0</u>	<u>0</u>	<u>0</u>	<u>3</u>
LSTM	<u>NSE</u>	<u>- 0.35</u>	<u>- 0.39</u>	<u>- 0.22</u>	<u>- 0.17</u>	<u>- 0.2</u>	<u>- 0.2</u>
	<u>KGE</u>	<u>0.3</u>	<u>0.05</u>	<u>0.18</u>	<u>0.34</u>	<u>0.33</u>	<u>0.4</u>
	<u>RMSE</u>	<u>1984</u>	<u>348</u>	<u>834</u>	<u>324</u>	<u>300</u>	<u>220</u>
	<u>MAE</u>	<u>1304</u>	<u>192</u>	<u>468</u>	<u>234</u>	<u>201</u>	<u>174</u>
	<u>PFE</u>	<u>0.24</u>	<u>0.36</u>	<u>0.42</u>	<u>0.6</u>	<u>0.44</u>	<u>0.42</u>
	<u>TPE (hours)</u>	<u>3</u>	<u>4</u>	<u>3</u>	<u>0</u>	<u>2</u>	<u>2</u>
	<u>P-Factor</u>	<u>36 %</u>	<u>79 %</u>	<u>90.3 %</u>	<u>85 %</u>	<u>86 %</u>	<u>63 %</u>
	<u>R-Factor</u>	<u>1.8</u>	<u>1.9</u>	<u>2.16</u>	<u>1.6</u>	<u>3.7</u>	<u>1.6</u>
	<u>TPE (hours)</u>	<u>3</u>	<u>4</u>	<u>3</u>	<u>0</u>	<u>2</u>	<u>2</u>

696

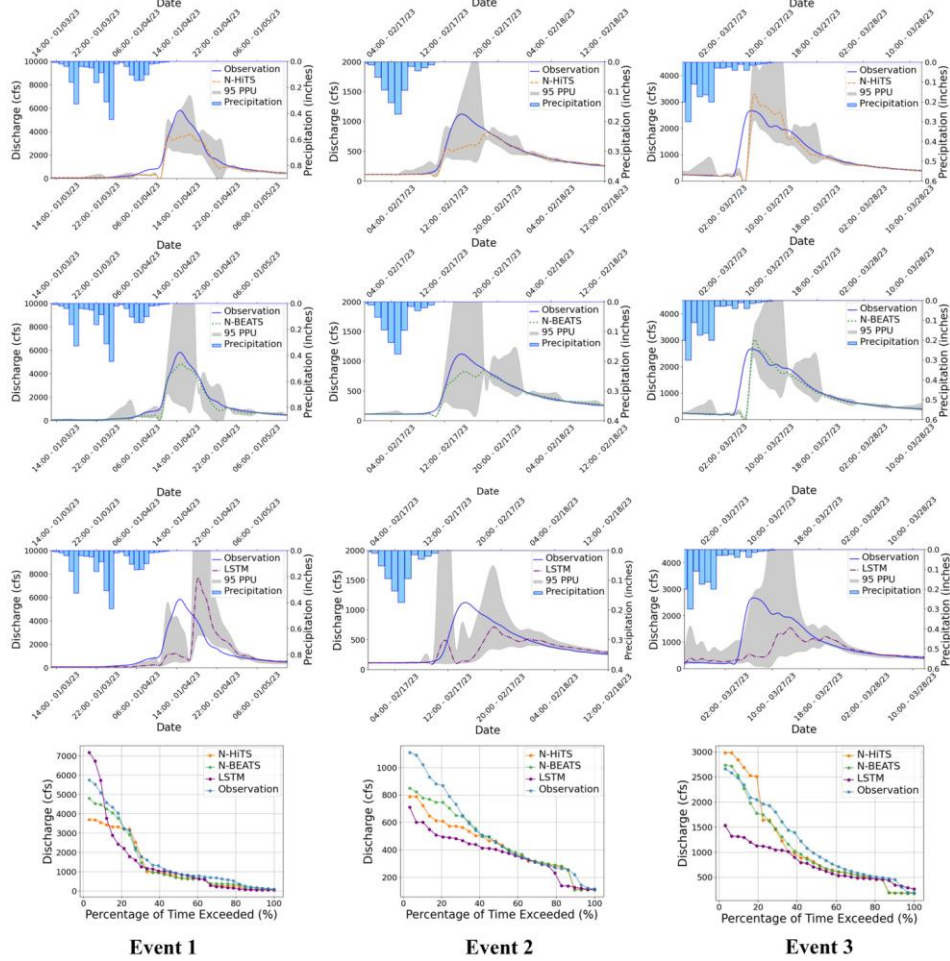


Event 1

Event 2

Event 3

Figure 9. 95 PPU band and FDC plots of N-HiTS, N-BEATS, and LSTM models with 3-hour prediction horizon for the three selected flooding events in the Lower Dog River gauging station.

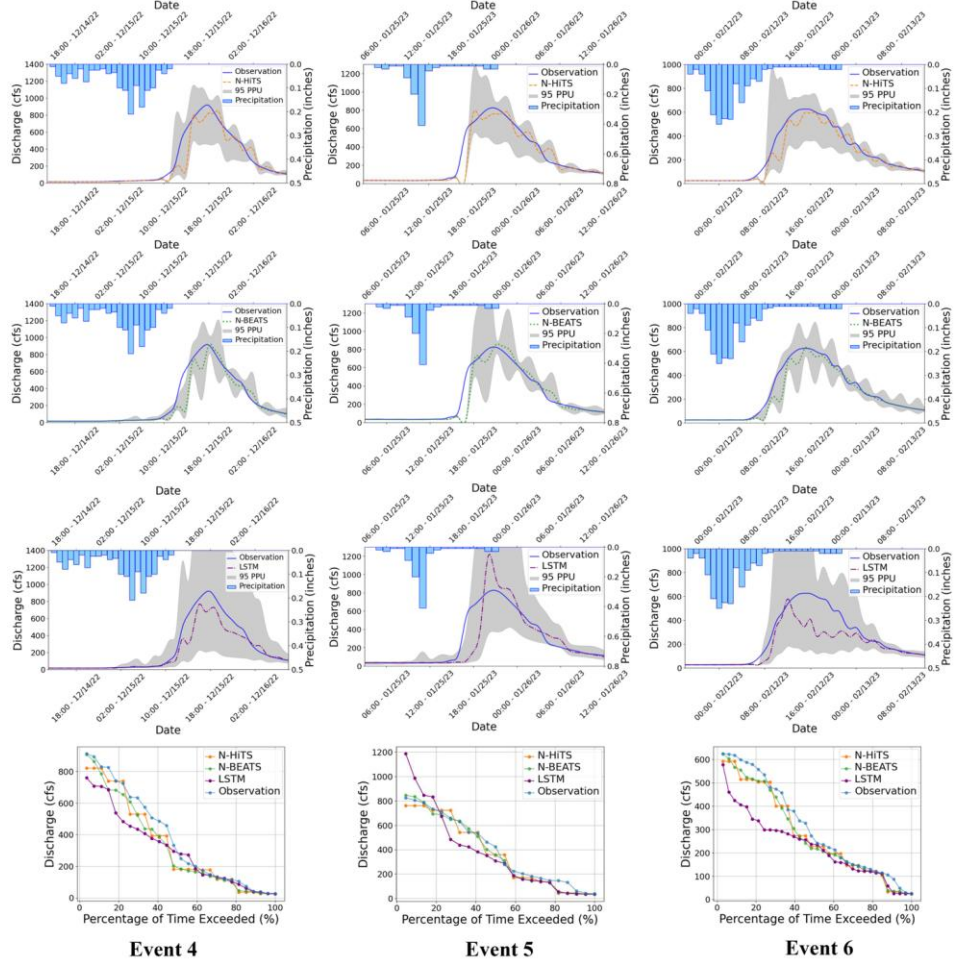


701

702

703

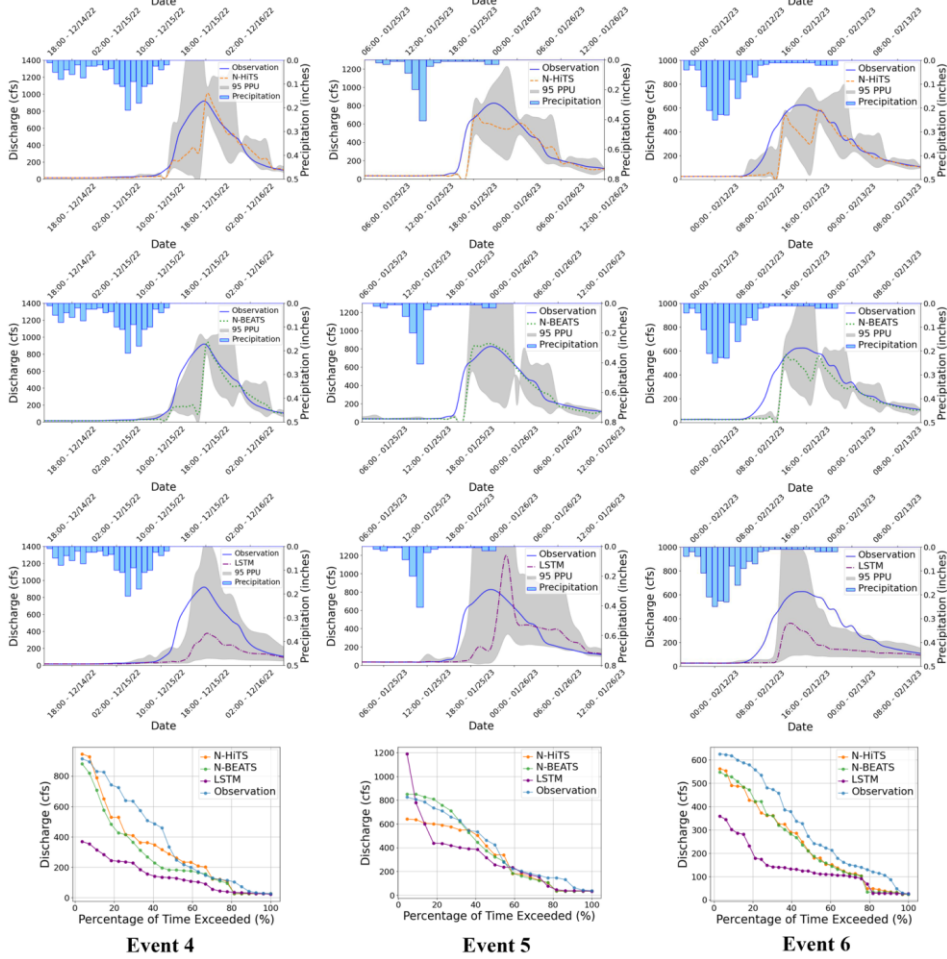
704



705

706
707

Figure 11. 95 PPU band and FDC plots of N-HiTS, N-BEATS, and LSTM models with 3-hour prediction horizon for the three selected flooding events in the Killian Creek gauging station.



708

709 [Figure 12. 95 PPU band and FDC plots of N-HiTS, N-BEATS, and LSTM models with 6-hour prediction](#)
 710 [horizon for the three selected flooding events in the Killian Creek gauging station.](#)

711

712 [To probe cross-catchment generalizability, we trained a single “regional” model by pooling Lower Dog](#)
 713 [River and Killian Creek, preserving per-site temporal splits and fitting a global scaler only on the pooled](#)
 714 [training portion to avoid leakage; evaluation remained strictly per site. Relative to per-site training, pooled](#)
 715 [fitting produced a small accuracy drop for N-HiTS and N-BEATS \(~ 2 to 3 %\). LSTM showed mixed](#)

Formatted: Font: (Default) +Headings CS (Times New Roman), 11 pt

Formatted: Font: (Default) +Headings CS (Times New Roman)

Formatted: Font: (Default) +Headings CS (Times New Roman), 11 pt

716 performance to pooling, it improved in some storm events but degraded in others, so that, when averaged
717 across both stations and storm events, its regional performance was effectively unchanged relative to the
718 per-site training. Despite that, the regional N-HiTS/N-BEATS matched the accuracy of the best per-site
719 models within the variability observed across storm events and, importantly, consistently surpassed LSTM
720 at both basins. Mechanically, N-HiTS's multi-rate pooling and hierarchical interpolation, and N-
721 BEATS's trend/seasonality basis projection, act as catchment-invariant feature extractors that support
722 parameter sharing across stations.

723 In our investigation, we conducted an analysis to assess the impact of varying input sizes on the performance
724 of the N-HiTS, as the best model. We implemented four different durations as input sizes to observe the
725 corresponding differences in modeling performance. Notably, one of the key metrics affected by changes
726 in input size was 95PPU, which exhibited a general decrease with increasing input size.

727 As detailed in Table 57, we observed a discernible trend in the R-Factor of the N-HiTS model as the input
728 size was increased. Specifically, there was a decline in the R-Factor as the input size expanded. This trend
729 underscores the influence of input size on model performance, particularly in terms of 95PPU band and
730 accuracy.

731 Overall, uncertainty analysis revealed that coupling MLE with N-HiTS and N-BEATS models
732 demonstrated superior performance in generating 95PPU, effectively reducing errors in flood prediction.
733 The MLE approach was more successful in reducing 95PPU bands of N-HiTS and N-BEATS models
734 compared to the LSTM, as indicated by the R-Factor and P-Factor. The N-BEATS model demonstrated a
735 narrower uncertainty band (lower R-Factor value), while the N-HiTS model provided higher precision.
736 Furthermore, incorporating data with various sizes into the N-HiTS model led to a narrower 95PPU and an
737 improvement in the R-Factor, highlighting the significance of input size in enhancing model accuracy and
738 reducing uncertainty.

Table 57. N-HiTS's R-Factor results for three storm events in each case study, using 1
hour, 6 hours, 12 hours, and 24 hours input size in training.

Input Size	1 hour	6 hours	12 hours	24 hours
Dog River, GA - Event 1	0.314	0.337	0.29	0.272
Dog River, GA - Event 2	0.35	0.413	0.403	0.402
Dog River, GA - Event 3	0.358	0.459	0.374	0.336
Killian Creek, NC - Event 4	0.491	0.422	0.426	0.388
Killian Creek, NC - Event 5	0.584	0.503	0.557	0.483

739 **Killian Creek, NC - Event 6** 0.482 0.42 0.446 0.454

740

3.4. Sensitivity Analysis

741 In this study, we conducted a comprehensive sensitivity analysis of the N-HiTS, N-BEATS, and LSTM
 742 models to evaluate their responsiveness to meteorological variables, specifically precipitation, humidity,
 743 and temperature. The goal was to assess how the omission of input ~~parameters features impacts impact~~ the
 744 overall modeling performance compared to their full-variable counterparts.

745 To execute this analysis, we systematically trained each model by excluding meteorological variables one
 746 or more at a time, subsequently evaluating their predictive performance using the entire testing dataset.
 747 The results of our analysis indicated that N-HiTS and N-BEATS models exhibited minimal sensitivity to
 748 meteorological variables, as evidenced by the negligible impact on their performance metric (i.e., NSE,
 749 Persistent-NSE, KGE, RMSE, and MAE) upon ~~input feature parameter~~ exclusion.

750 Notably, as shown in Table 68, the performance of the N-HiTS model displayed a marginal deviation
 751 under variable omission, while the N-BEATS model exhibited consistent performance irrespective of the
 752 inclusion or exclusion of meteorological variables. The structure of this algorithm is based on backward
 753 and forward residual links for univariate time series point forecasting which does not take into account
 754 other ~~input features parameters~~ in the prediction task. These findings suggest that the predictive
 755 capabilities of N-HiTS and N-BEATS models predominantly rely on historical flood data. Both models
 756 demonstrated strong performance even without incorporating precipitation, temperature, or humidity data,
 757 underscoring their ability in flood prediction in the absence of specific meteorological inputs. This
 758 capability underscores the robustness of the N-HiTS and N-BEATS models, positioning them as viable
 759 tools and perhaps appropriate for real-time flood forecasting tasks where direct meteorological data may
 760 be limited or unavailable.

761

762 Table 68. Performance metrics' values for N-HiTS, N-BEATS, and LSTM models by excluding
 763 meteorological variables one or more at a time.

Model	Excluded Variables	NSE	Persistent-NSE	KGE	RMSE	MAE
N-HiTS	Using all variables	0.996	0.92	0.988	22.66	4.19
	Without Precipitation	0.993	0.91	0.97	23.28	4.31
	Without Humidity	0.995	0.914	0.976	22.87	4.22

	Without Temperature	0.995	0.921	0.985	22.43	4.14
	Discharge only prediction	0.993	0.911	0.972	23.21	4.29
	Using all variables	0.994	0.978	0.992	11.80	2.13
	Without Precipitation	0.994	0.978	0.991	11.86	2.17
N-BEATS	Without Humidity	0.994	0.978	0.991	11.81	2.16
	Without Temperature	0.994	0.978	0.991	11.82	2.16
	Discharge only prediction	0.994	0.978	0.991	11.96	2.17
	Using all variables	0.992	0.865	0.926	29.52	8.15
	Without Precipitation	0.979	0.665	0.892	39.46	19.83
LSTM	Without Humidity	0.991	0.843	0.925	31.73	9.15
	Without Temperature	0.983	0.628	0.872	48.95	11.49
	Discharge only prediction	0.976	0.576	0.692	52.28	33.5

764

765 **3.5 Computational Efficiency**

766 The computational efficiency of the N-HiTS, N-BEATS, and LSTM models, as well as a comparative
 767 analysis, is presented in Table 79. The study encompassed the entire process of training and predicting over
 768 the testing period, employing the optimized hyperparameters as previously described. Regarding the
 769 training time, it is noteworthy that the LSTM model exhibited the quickest performance. Specifically,
 770 LSTM demonstrated a training time that was 71% faster than N-HiTS and 93% faster than N-BEATS in
 771 the Lower Dog River watershed, while it was respectively, 126% and 118% faster than N-HiTS and N-
 772 BEATS in the Upper Dutchmans Creek, over training dataset. This is because LSTM has a simple
 773 architecture compared to the N-BEATS and N-HiTS and does not require multivariate features, hierarchical

774 interpolation, and multi-rate data sampling. Perhaps, this outcome underscores the computational advantage
775 of LSTM over other algorithms.

776 Conversely, during the testing period, the N-HiTS model emerged as the fastest and delivered the most
777 efficient results in comparison to the other models. Notably, N-HiTS displayed a predicting time that was
778 33% faster than LSTM and 32% faster than N-BEATS. This finding highlights the computational efficiency
779 of the N-HiTS model in the context of predicting processes. Our experiments unveiled an interesting
780 contrast in the computational performance of these models. While LSTM excelled in terms of training time,
781 it lagged behind when it came to the testing period.

782 In the grand scheme of computational efficiency, model accuracy, and uncertainty analysis results, it
783 becomes evident that the superiority of the N-HiTS and N-BEATS models in terms of accuracy and
784 uncertainty analysis holds paramount importance. This significance is accentuated by the critical nature of
785 flood prediction, where precision and certainty are pivotal. Therefore, computational efficiency must be
786 viewed in the context of the broader objectives, with the accuracy and reliability of flood predictions taking
787 precedence in ensuring the safety and preparedness of the affected regions.

788

789 Table 79. Computational costs of N-HiTS, N-BEATS, and LSTM models in the Dog River and Killian
790 Creek gauging stations.

Model	Training Time over Train Datasets		Predicting Time over Test Datasets	
	Lower Dog River	Upper Dutchmans Creek	Lower Dog River	Upper Dutchmans Creek
N-HiTS	256.032	374.569	1533.029	1205.526
N-BEATS	288.511	361.599	2028.068	1482.305
LSTM	149.173	165.827	2046.140	1792.444

791

792 4. Conclusion

793 This study examined multiple NN algorithms for flood prediction. We selected two headwater streams with
794 minimal human impacts to understand how NN approaches can capture flood magnitude and timing for
795 these natural systems. In conclusion, our study represents a pioneering effort in exploring and advancing
796 the application of NN algorithms, specifically the N-HiTS and N-BEATS models, in the field of flood
797 prediction. In our case studies, both N-HiTS and N-BEATS models achieved state-of-the-art results,
798 outperforming LSTM as a benchmark model, particularly in one-hour prediction. While a one-hour lead
799 time may seem brief, it is highly significant for accurate flash flood prediction particularly ~~in an~~ in an area

800 with a proximity to large metropolitan cities, where rapid response is critical. These benchmarking results
801 are arguably a pivotal part of this research. However, the N-BEATS model slightly emerged as a powerful
802 and interpretable tool for flood prediction in most selected events.

803 This study focused on short-lead, operational forecasting at gauged sites, using historical discharge to
804 deliver robust, low-latency updates. While the evaluation is limited to two southeastern U.S. basins, the
805 architecture (e.g., N-HiTS) is flexible and can incorporate additional covariates and catchment attributes.
806 Extending the approach to ungauged or other basins is feasible through multi-basin training and transfer
807 learning or few-shot adaptation when even brief warm-up records are available. These extensions represent
808 promising directions for future work to assess geographic transferability under the same operational
809 assumptions.

810 This research targeted short lead prediction at operationally gauged sites, leveraging historical discharge to
811 provide robust, low latency updates. However, the architectures (i.e. N-HiTS) readily accept additional
812 covariates and inputs. The work can be extended to ungauged basins by multi-basin training with catchment
813 attributes, and transfer or few-shot adaptation when brief warm-up records exist.

814 In addition, the results of the experiments described above demonstrated that N-HiTS multi-rate input
815 sampling and hierarchical interpolation along with N-BEATS interpretable configuration are effective in
816 learning location-specific runoff generation behaviors. Both algorithms with an MLP-based deep neural
817 architecture with backward and forward residual links can sequentially project the data signal into
818 polynomials and harmonic basis needed to predict intense storm behaviors with varied magnitudes. The
819 innovation in this study—besides benchmarking the LSTM model for headwater streams—was to tackle
820 volatility and memory complexity challenges, by locally specializing flood sequential predictions into the
821 data signal's frequencies with interpretability, and hierarchical interpolation and pooling. Both N-HiTS and
822 N-BEATS models offered similar performance as compared with the LSTM but also offered a level of
823 interpretability about how the model learns to differentiate aspects of complex watershed-specific behaviors
824 via data. The interpretability of N-HiTS and N-BEATS arises directly from their model architecture. In the
825 interpretable N-BEATS framework, forecasts are decomposed into trend and seasonality stacks, each
826 represented by explicit basis coefficients that reveal how different temporal patterns contribute to the
827 prediction. Similarly, N-HiTS achieves interpretability by aggregating contributions across multiple distinct
828 time scales, allowing insight into the temporal dynamics driving each forecast. The interpretability of N-
829 HiTS and N-BEATS models stems from their designs. The interpretable N-BEATS architecture
830 decomposes forecasts into trend and seasonality stacks with explicit basis coefficients, and N-HiTS forms
831 predictions by aggregating contributions across distinct time scales. N-HiTS aims to enhance the accuracy
832 of long-term time-series forecasts through hierarchical interpolation and multi-scale data sampling,
833 allowing it to focus on different data patterns, which prioritizes features essential to understand flood

834 magnitudes. N-BEATS leverages interpretable configurations with trend and seasonality projections,
835 enabling it to decompose time series data into intuitive components. N-BEATS interpretable architecture
836 is recommended for scarce data settings (such as flooding event), as it regularizes its predictions through
837 projections unto harmonic and trend basis. These approaches improve model transparency by allowing
838 understanding of how each part of the model contributes to the final prediction, particularly when applied
839 to complex flood patterns. Both models also support multivariate series (and covariates) by flattening the
840 model inputs to a 1-D series and reshaping the outputs to a tensor of appropriate dimensions. This approach
841 provides flexibility to handle arbitrary numbers of features. Furthermore, both N-HiTS and N-BEATS
842 ~~models~~—models, like LSTM, also support producing probabilistic predictions by specifying a likelihood
843 ~~parameter~~—objective. In terms of sensitivity analysis, both N-HiTS and N-BEATS models maintain
844 consistent performance even when trained without specific meteorological inputs. Although, during some
845 flashy floods, the models encountered challenges in capturing the peak flows and the dynamics of the
846 recession curve, which is directly related to groundwater contribution to flood hydrograph, both models
847 were technically insensitive to rainfall data as an input variable. This suggests the fact that both algorithms
848 can learn patterns in discharge data without requiring meteorological input. This ability underscores these
849 models' robustness in generating accurate predictions using historical flood data alone, making them
850 valuable tools for flood prediction, especially in data-poor watersheds or even for real-time flood prediction
851 when near real-time meteorological inputs are limited or unavailable. In terms of computational efficiency,
852 both N-HiTS and N-BEATS are trained almost at the same pace; however, N-HiTS predicted the test data
853 much quicker than N-BEATS. Unlike N-HiTS and N-BEATS, LSTM excelled in reducing training time
854 due to its simplicity and limited number of parameters.

855 Moving forward, it is worth mentioning that predicting the magnitude of the recession curve of flood
856 hydrographs was particularly challenging for all models. We argue that this is because the relation between
857 base flow and time is particularly hard to calibrate due to ground-water effluent that is controlled by
858 geological and physical conditions (vegetation, wetlands, wet meadows) in headwater streams. In addition,
859 the situations of runoff occurrence are diverse and have a high measurement variance with high frequency
860 that can make it difficult for the algorithms to fully capture discrete representation learning on time series.
861 In future studies, it will be important to develop strategies to derive analogs to the interpretable
862 configuration as well as multi-rate input sampling, hierarchical interpolation, and backcast residual
863 connections that allow for the dynamic representation of flood times series data with different frequencies
864 and nonlinearity. A dynamic representation of flood time series is, at least in principle, possible by
865 generating additive predictions in different bands of the time-series signals, reducing memory footprint and
866 compute time, and improving architecture parsimony and accuracy. This would allow the model to “learn”
867 interpretability and hierarchical representations from raw data to reduce complexity as the information

868 flows through the network. Moreover, it is noteworthy that while a single station offers valuable localized
869 data, particularly for smaller watersheds such as headwater streams where runoff is closely tied to
870 immediate meteorological conditions, it may not fully capture the spatial heterogeneity of larger
871 watersheds. [The work was mainly for a capability test in an hourly, operational setting in the southeastern basins.](#) For our specific case, the methods applied herein captured runoff magnitude and dynamics in small
872 watersheds using a single station. However, we recognize that for broader areas, incorporating spatially
873 distributed data would likely enhance model accuracy. [Conclusions are scoped to these basins and horizons; broader generalization will require multi-region in future work.](#) Lastly, one could explore the idea of
874 enhancing N-HiTS and N-BEATS (or NN algorithms, in general) performance with uncertainty
875 quantification by using more robust Bayesian inference such as Bayesian Model Averaging (BMA) with
876 fixed and flexible prior distributions (see Samadi et al., 2020) and/or Markov Chain Monte-Carlo
877 optimization methods (Duane et al., 1987) addressing both aleatoric and epistemic uncertainties. We leave
878 these approaches for future discussion and exploration in the context of flood neural time series prediction.
879
880

881 5. Acknowledgements

882 This research is supported by the US National Science Foundation Directorate of Engineering (Grant #
883 CMMI 2125283). All opinions, findings, and conclusions or recommendations expressed in this material
884 are those of the authors and do not necessarily reflect the views of the NSF. The authors acknowledge and
885 appreciate Thorsten Wagener (University of [University of Potsdam](#), Germany) discussion and feedback on
886 this manuscript. Clemson University (USA) is acknowledged for generous allotment of computing time on
887 the Palmetto cluster.
888

889 6. Open Research

890 The historical discharge data used in this study are from the USGS
891 (https://waterdata.usgs.gov/nwis/uv/?referred_module=sw), meteorological data from USDA
892 (<https://www.ncdc.noaa.gov/cdo-web/datatools/lcd>). We have uploaded the datasets and codes
893 used in this research to Zenodo, accessible via <https://zenodo.org/records/13343364>. For
894 modeling, we used the NeuralForecast package (Olivares et al., 2022), available at:
895 <https://github.com/Nixtla/neuralforecast>.
896

897 7. References

Formatted: Font: (Default) +Headings CS (Times New Roman), 11 pt
Formatted: Font: (Default) +Headings CS (Times New Roman), 11 pt
Formatted: Font: 11 pt

- 899 Abbaspour, K.C., Yang, J., Maximov, I., Siber, R., Bogner, K., Mieleitner, J., Zobrist, J., Srinivasan, R.,
900 2007. Modelling hydrology and water quality in the pre-alpine/alpine Thur watershed using SWAT.
901 *Journal of Hydrology* 333, 413–430. <https://doi.org/10.1016/j.jhydrol.2006.09.014>
- 902 Alaa, A.M., van der Schaar, M., 2019. Attentive State-Space Modeling of Disease Progression, in:
903 *Advances in Neural Information Processing Systems*. Curran Associates, Inc.
- 904 Asquith, W.H., Roussel, M.C., Thompson, D.B., Cleveland, T.G., Fang, X., 2005. Summary of
905 dimensionless Texas hyetographs and distribution of storm depth developed for Texas Department
906 of Transportation research project 0-4194 (No. 0-4194-4). Texas Department of Transportation.
- 907 Barnard, P.L., van Ormondt, M., Erikson, L.H., Eshleman, J., Hapke, C., Ruggiero, P., Adams, P.N.,
908 Foxgrover, A.C., 2014. Development of the Coastal Storm Modeling System (CoSMoS) for
909 predicting the impact of storms on high-energy, active-margin coasts. *Nat Hazards* 74, 1095–1125.
910 <https://doi.org/10.1007/s11069-014-1236-y>
- 911 Basso, S., Schirmer, M., Botter, G., 2016. A physically based analytical model of flood frequency curves.
912 *Geophysical Research Letters* 43, 9070–9076. <https://doi.org/10.1002/2016GL069915>
- 913 Challu, C., Olivares, K.G., Oreshkin, B.N., Garza, F., Mergenthaler-Canseco, M., Dubrawski, A., 2022.
914 N-HiTS: Neural Hierarchical Interpolation for Time Series Forecasting.
915 <https://doi.org/10.48550/arXiv.2201.12886>
- 916 Chen, Y., Li, J., Xu, H., 2016. Improving flood forecasting capability of physically based distributed
917 hydrological models by parameter optimization. *Hydrology and Earth System Sciences* 20, 375–
918 392. <https://doi.org/10.5194/hess-20-375-2016>
- 919 Clark, M.P., Nijssen, B., Lundquist, J.D., Kavetski, D., Rupp, D.E., Woods, R.A., Freer, J.E., Gutmann,
920 E.D., Wood, A.W., Brekke, L.D., Arnold, J.R., Gochis, D.J., Rasmussen, R.M., 2015. A unified
921 approach for process-based hydrologic modeling: 1. Modeling concept. *Water Resources Research*
922 51, 2498–2514. <https://doi.org/10.1002/2015WR017198>
- 923 CRED, n.d. EM-DAT - The international disaster database [WWW Document]. URL
924 <https://www.emdat.be/> (accessed 6.5.24).
- 925 Dasgupta, A., Arnal, L., Emerton, R., Harrigan, S., Matthews, G., Muhammad, A., O'Regan, K., Pérez-
926 Ciria, T., Valdez, E., van Osnabrugge, B., Werner, M., Buontempo, C., Cloke, H., Pappenberger,
927 F., Pechlivanidis, I.G., Prudhomme, C., Ramos, M.-H., Salamon, P., n.d. Connecting hydrological
928 modelling and forecasting from global to local scales: Perspectives from an international joint
929 virtual workshop. *Journal of Flood Risk Management* n/a, e12880.
930 <https://doi.org/10.1111/jfr3.12880>
- 931 Defontaine, T., Ricci, S., Lapeyre, C., Marchandise, A., Pape, E.L., 2023. Flood forecasting with Machine
932 Learning in a scarce data layout. *IOP Conf. Ser.: Earth Environ. Sci.* 1136, 012020.
933 <https://doi.org/10.1088/1755-1315/1136/1/012020>

- 934 Duane, S., Kennedy, A.D., Pendleton, B.J., Roweth, D., 1987. Hybrid Monte Carlo. Physics Letters B
935 195, 216–222. [https://doi.org/10.1016/0370-2693\(87\)91197-X](https://doi.org/10.1016/0370-2693(87)91197-X)
- 936 Erikson, L.H., Espejo, A., Barnard, P.L., Serafin, K.A., Hegermiller, C.A., O'Neill, A., Ruggiero, P.,
937 Limber, P.W., Mendez, F.J., 2018. Identification of storm events and contiguous coastal sections
938 for deterministic modeling of extreme coastal flood events in response to climate change. Coastal
939 Engineering 140, 316–330. <https://doi.org/10.1016/j.coastaleng.2018.08.003>
- 940 Evin, G., Le Lay, M., Fouchier, C., Mas, A., Colleoni, F., Penot, D., Garambois, P.-A., Laurantin, O.,
941 2023. Evaluation of hydrological models on small mountainous catchments: impact of the
942 meteorological forcings. <https://doi.org/10.5194/egusphere-2023-845>
- 943 Fan, C., Zhang, Y., Pan, Y., Li, X., Zhang, C., Yuan, R., Wu, D., Wang, W., Pei, J., Huang, H., 2019.
944 Multi-Horizon Time Series Forecasting with Temporal Attention Learning, in: Proceedings of the
945 25th ACM SIGKDD International Conference on Knowledge Discovery & Data Mining, KDD '19.
946 Association for Computing Machinery, New York, NY, USA, pp. 2527–2535.
947 <https://doi.org/10.1145/3292500.3330662>
- 948 Fang, K., Kifer, D., Lawson, K., Shen, C., 2020. Evaluating the Potential and Challenges of an
949 Uncertainty Quantification Method for Long Short-Term Memory Models for Soil Moisture
950 Predictions. Water Resources Research 56, e2020WR028095.
951 <https://doi.org/10.1029/2020WR028095>
- 952 Global assessment report on disaster risk reduction 2015 | UNDRR, 2015. URL:
953 <http://www.undrr.org/publication/global-assessment-report-disaster-risk-reduction-2015> (accessed
954 6.5.24).
- 955 Gotvald, A.J., 2010. Historic flooding in Georgia, 2009: U.S. Geological Survey Open-File Report 2010–
956 1230, 19 p.
- 957 Gupta, H.V., Kling, H., Yilmaz, K.K., Martinez, G.F., 2009. Decomposition of the mean squared error
958 and NSE performance criteria: Implications for improving hydrological modelling. Journal of
959 Hydrology 377, 80–91. <https://doi.org/10.1016/j.jhydrol.2009.08.003>
- 960 Hochreiter, S., Younger, A.S., Conwell, P.R., 2001. Learning to Learn Using Gradient Descent, in:
961 Dorffner, G., Bischof, H., Hornik, K. (Eds.), Artificial Neural Networks — ICANN 2001. Springer,
962 Berlin, Heidelberg, pp. 87–94. https://doi.org/10.1007/3-540-44668-0_13
- 963 Hsu, K., Gupta, H.V., Sorooshian, S., 1995. Artificial Neural Network Modeling of the Rainfall-Runoff
964 Process. Water Resources Research 31, 2517–2530. <https://doi.org/10.1029/95WR01955>
- 965 Jonkman, S.N., 2005. Global Perspectives on Loss of Human Life Caused by Floods. Nat Hazards 34,
966 151–175. <https://doi.org/10.1007/s11069-004-8891-3>
- 967 Kingma, D.P., Ba, J., 2017. Adam: A Method for Stochastic Optimization.
968 <https://doi.org/10.48550/arXiv.1412.6980>

- 969 Kratzert, F., Klotz, D., Brenner, C., Schulz, K., Herrnegger, M., 2018. Rainfall–runoff modelling using
970 Long Short-Term Memory (LSTM) networks. *Hydrology and Earth System Sciences* 22, 6005–
971 6022. <https://doi.org/10.5194/hess-22-6005-2018>
- 972 Lim, B., Arik, S.Ö., Loeff, N., Pfister, T., 2021. Temporal Fusion Transformers for interpretable multi-
973 horizon time series forecasting. *International Journal of Forecasting* 37, 1748–1764.
974 <https://doi.org/10.1016/j.ijforecast.2021.03.012>
- 975 Lobligeois, F., Andréassian, V., Perrin, C., Tabary, P., Loumagne, C., 2014. When does higher spatial
976 resolution rainfall information improve streamflow simulation? An evaluation using 3620 flood
977 events. *Hydrology and Earth System Sciences* 18, 575–594. <https://doi.org/10.5194/hess-18-575-2014>
- 979 MacDonald, L.H., Coe, D., 2007. Influence of Headwater Streams on Downstream Reaches in Forested
980 Areas. *Forest Science* 53, 148–168. <https://doi.org/10.1093/forestscience/53.2.148>
- 981 Martinaitis, S.M., Wilson, K.A., Yussouf, N., Gourley, J.J., Vergara, H., Meyer, T.C., Heinselman, P.L.,
982 Gerard, A., Berry, K.L., Vergara, A. and Monroe, J., 2023. A path toward short-term probabilistic
983 flash flood prediction. *Bulletin of the American Meteorological Society*, 104(3), pp.E585–E605.
- 984 McCallum, B.E., and Gotvald, A.J., 2010, Historic flooding in northern Georgia, September 16–22, 2009:
985 U.S. Geological Survey Fact Sheet 2010–3061, 4 p.
- 986 McCuen, R.H., Knight, Z., Cutter, A.G., 2006. Evaluation of the Nash–Sutcliffe Efficiency Index. *Journal*
987 *of Hydrologic Engineering* 11, 597–602. [https://doi.org/10.1061/\(ASCE\)1084-0699\(2006\)11:6\(597\)](https://doi.org/10.1061/(ASCE)1084-0699(2006)11:6(597)
- 989 Munn, M., Sheibley, R., Waite, I., Meador, M., 2020. Understanding the relationship between stream
990 metabolism and biological assemblages. *Freshwater Science* 39, 680–692.
991 <https://doi.org/10.1086/711690>
- 992 Nash, J.E., Sutcliffe, J.V., 1970. River flow forecasting through conceptual models part I — A discussion
993 of principles. *Journal of Hydrology* 10, 282–290. [https://doi.org/10.1016/0022-1694\(70\)90255-6](https://doi.org/10.1016/0022-1694(70)90255-6)
- 994 Nevo, S., Morin, E., Gerzi Rosenthal, A., Metzger, A., Barshai, C., Weitzner, D., Voloshin, D., Kratzert,
995 F., Elidan, G., Dror, G., Begelman, G., Nearing, G., Shalev, G., Noga, H., Shavitt, I., Yuklea, L.,
996 Royz, M., Giladi, N., Peled Levi, N., Reich, O., Gilon, O., Maor, R., Timnat, S., Shechter, T.,
997 Anisimov, V., Gigi, Y., Levin, Y., Moshe, Z., Ben-Haim, Z., Hassidim, A., Matias, Y., 2022. Flood
998 forecasting with machine learning models in an operational framework. *Hydrology and Earth*
999 *System Sciences* 26, 4013–4032. <https://doi.org/10.5194/hess-26-4013-2022>
- 1000 NRCS (2009). Part 630 Hydrology National Engineering Handbook, Chapter 15: Time of Concentration.
- 1001 Olivares, K. G., Challú, C., Garza, F., Mergenthaler Canseco, M., & Dubrawski, A. (2022).
1002 NeuralForecast: User friendly state-of-the-art neural forecasting models. PyCon Salt Lake City,
1003 Utah, US 2022. Retrieved from <https://github.com/Nixtla/neuralforecast>

- 1004 Olivares, K.G., Meetei, O.N., Ma, R., Reddy, R., Cao, M., Dicker, L., 2024. Probabilistic hierarchical
1005 forecasting with deep Poisson mixtures. *International Journal of Forecasting* 40, 470–489.
1006 <https://doi.org/10.1016/j.ijforecast.2023.04.007>
- 1007 Oreshkin, B.N., Carpov, D., Chapados, N., Bengio, Y., 2020. N-BEATS: Neural basis expansion analysis
1008 for interpretable time series forecasting. <https://doi.org/10.48550/arXiv.1905.10437>
- 1009 Pally, R.J., Samadi, V., 2021. Application of image processing and convolutional neural networks for
1010 flood image classification and semantic segmentation. *Environmental Modelling & Software* 148,
1011 105285. <https://doi.org/10.1016/j.envsoft.2021.105285>
- 1012 Palmer, T.N., 2012. Towards the probabilistic Earth-system simulator: a vision for the future of climate
1013 and weather prediction. *Quarterly Journal of the Royal Meteorological Society* 138, 841–861.
1014 <https://doi.org/10.1002/qj.1923>
- 1015 Park, K., Lee, E.H., 2024. Urban flood vulnerability analysis and prediction based on the land use using
1016 Deep Neural Network. *International Journal of Disaster Risk Reduction* 101, 104231.
1017 <https://doi.org/10.1016/j.ijdrr.2023.104231>
- 1018 Pourreza-Bilondi, M., Samadi, S.Z., Akhoond-Ali, A.-M., Ghahraman, B., 2017. Reliability of Semiarid
1019 Flash Flood Modeling Using Bayesian Framework. *Journal of Hydrologic Engineering* 22,
1020 05016039. [https://doi.org/10.1061/\(ASCE\)HE.1943-5584.0001482](https://doi.org/10.1061/(ASCE)HE.1943-5584.0001482)
- 1021 Refsgaard, J.C., Stisen, S., Koch, J., 2022. Hydrological process knowledge in catchment modelling –
1022 Lessons and perspectives from 60 years development. *Hydrological Processes* 36, e14463.
1023 <https://doi.org/10.1002/hyp.14463>
- 1024 Roelvink, D., Reniers, A., van Dongeren, A., van Thiel de Vries, J., McCall, R., Lescinski, J., 2009.
1025 Modelling storm impacts on beaches, dunes and barrier islands. *Coastal Engineering* 56, 1133–
1026 1152. <https://doi.org/10.1016/j.coastaleng.2009.08.006>
- 1027 Russo, S., Perraquin, N., Stalder, S., Perez-Cruz, F., Leitao, J.P., Obozinski, G., Wegner, J.D., 2023. An
1028 evaluation of deep learning models for predicting water depth evolution in urban floods.
1029 <https://doi.org/10.48550/arXiv.2302.10062>
- 1030 Saberian, M., Zafarmomen, N., Neupane, A., Panthi, K., Samadi, V., 2025. HydroQuantum: A New
1031 Quantum-driven Python Package for Hydrological Simulation. *Environmental Modelling &*
1032 *Software* 106736. <https://doi.org/10.1016/j.envsoft.2025.106736>
- 1033 Safaei-Moghadam, A., Tarboton, D., Minsker, B., 2023. Estimating the likelihood of roadway pluvial
1034 flood based on crowdsourced traffic data and depression-based DEM analysis. *Natural Hazards and*
1035 *Earth System Sciences* 23, 1–19. <https://doi.org/10.5194/nhess-23-1-2023>
- 1036 Saksena, S., Dey, S., Merwade, V., Singhofen, P.J., 2020. A Computationally Efficient and Physically
1037 Based Approach for Urban Flood Modeling Using a Flexible Spatiotemporal Structure. *Water*
1038 *Resources Research* 56, e2019WR025769. <https://doi.org/10.1029/2019WR025769>

- 1039 Samadi, S., Pourreza-Bilondi, M., Wilson, C. a. M.E., Hitchcock, D.B., 2020. Bayesian Model Averaging
1040 With Fixed and Flexible Priors: Theory, Concepts, and Calibration Experiments for Rainfall-Runoff
1041 Modeling. *Journal of Advances in Modeling Earth Systems* 12, e2019MS001924.
1042 <https://doi.org/10.1029/2019MS001924>
- 1043 Samadi, V., Fowler, H.J., Lamond, J., Wagener, T., Brunner, M., Gourley, J., Moradkhani, H., Popescu,
1044 I., Wasko, C., Wright, D., Wu, H., Zhang, K., Arias, P.A., Duan, Q., Nazemi, A., van Oevelen, P.J.,
1045 Prein, A.F., Roundy, J.K., Saberian, M., Umutoni, L., 2025. The Needs, Challenges, and Priorities
1046 for Advancing Global Flood Research. *WIREs Water* 12, e70026.
1047 <https://doi.org/10.1002/wat2.70026>
- 1048 Scott, J., n.d. Widespread Flooding After Severe Storms - WCCB Charlotte's CW. Available at:
1049 <https://www.wccbcharlotte.com/2020/02/08/widespread-flooding-after-severe-storms/> (accessed
1050 6.11.24).
- 1051 Sukovich, E.M., Ralph, F.M., Barthold, F.E., Reynolds, D.W., Novak, D.R., 2014. Extreme Quantitative
1052 Precipitation Forecast Performance at the Weather Prediction Center from 2001 to 2011. *Weather
1053 and Forecasting* 29, 894–911. <https://doi.org/10.1175/WAF-D-13-00061.1>
- 1054 Tabas, S.S., Samadi, S., 2022. Variational Bayesian dropout with a Gaussian prior for recurrent neural
1055 networks application in rainfall–runoff modeling. *Environ. Res. Lett.* 17, 065012.
1056 <https://doi.org/10.1088/1748-9326/ac7247>
- 1057 Thompson, C.M., Frazier, T.G., 2014. Deterministic and probabilistic flood modeling for contemporary
1058 and future coastal and inland precipitation inundation. *Applied Geography* 50, 1–14.
1059 <https://doi.org/10.1016/j.apgeog.2014.01.013>
- 1060 Tiwari, M.K., Chatterjee, C., 2010. Development of an accurate and reliable hourly flood forecasting
1061 model using wavelet-bootstrap-ANN (WBANN) hybrid approach. *Journal of Hydrology* 394, 458–
1062 470. <https://doi.org/10.1016/j.jhydrol.2010.10.001>
- 1063 Watershed Report | Office of Water | US EPA, n.d. Available at:
1064 <https://watersgeo.epa.gov/watershedreport/?comid=9224629> (accessed 6.9.24).
- 1065 Wee, G., Chang, L.-C., Chang, F.-J., Mat Amin, M.Z., 2023. A flood Impact-Based forecasting system by
1066 fuzzy inference techniques. *Journal of Hydrology* 625, 130117.
1067 <https://doi.org/10.1016/j.jhydrol.2023.130117>
- 1068 Windheuser, L., Karanjit, R., Pally, R., Samadi, S., Hubig, N.C., 2023. An End-To-End Flood Stage
1069 Prediction System Using Deep Neural Networks. *Earth and Space Science* 10, e2022EA002385.
1070 <https://doi.org/10.1029/2022EA002385>
- 1071 Zafarmomen, N., Alizadeh, H., Bayat, M., Ehtiat, M., Moradkhani, H., 2024. Assimilation of Sentinel-
1072 Based Leaf Area Index for Modeling Surface-Ground Water Interactions in Irrigation Districts.
1073 *Water Resources Research* 60, e2023WR036080. <https://doi.org/10.1029/2023WR036080>

1074 Zafarmomen, N., Samadi, V., 2025. Can large language models effectively reason about adverse weather
1075 conditions? *Environmental Modelling & Software* 188, 106421.
1076 <https://doi.org/10.1016/j.envsoft.2025.106421>

1077 Zhang, L., Qin, H., Mao, J., Cao, X., Fu, G., 2023. High temporal resolution urban flood prediction using
1078 attention-based LSTM models. *Journal of Hydrology* 620, 129499.
1079 <https://doi.org/10.1016/j.jhydrol.2023.129499>

1080 Zhang, Y., Pan, D., Griensven, J.V., Yang, S.X., Gharabaghi, B., 2023. Intelligent flood forecasting and
1081 warning: a survey. *ir* 3, 190–212. <https://doi.org/10.20517/ir.2023.12>

1082 Zou, Y., Wang, J., Lei, P., Li, Y., 2023. A novel multi-step ahead forecasting model for flood based on time
1083 residual LSTM. *Journal of Hydrology* 620, 129521. <https://doi.org/10.1016/j.jhydrol.2023.129521>

1084